Scattering Interference Signature of a Pair Density Wave State in the Cuprate Pseudogap Phase

Shuqiu Wang[1§], Peayush Choubey[2,3§], Yi Xue Chong[4§], Weijiong Chen[1], Wangping Ren[1], H. Eisaki[6], S. Uchida[6], P.J. Hirschfeld[7] and J.C. Séamus Davis[1,4,5,8*]

1. *Clarendon Laboratory, University of Oxford, Oxford, OX1 3PU, UK*
2. *Institut für Theoretische Physik III, Ruhr-Universität Bochum, D-44801 Bochum, Germany.*
3. *Department of Physics, Indian Institute of Technology (Indian School of Mines), Dhanbad, Jharkhand-826004, India.*
4. *LASSP, Department of Physics, Cornell University, Ithaca NY 14850, USA*
5. *Department of Physics, University College Cork, Cork T12 R5C, Ireland*
6. *Inst. of Advanced Industrial Science and Tech., Tsukuba, Ibaraki 305-8568, Japan.*
7. *Department of Physics, University of Florida, Gainesville, FL, USA*
8. *Max-Planck Institute for Chemical Physics of Solids, D-01187 Dresden, Germany*

§ *These authors contributed equally to this project.*

* *Correspondence and requests for materials should be addressed to J.C.S.D. (email: jcseamusdavis@gmail.com)*

Abstract

An unidentified quantum fluid designated the pseudogap (PG) phase is produced by electron-density depletion in the CuO_2 antiferromagnetic insulator. Current theories suggest that the PG phase may be a pair density wave (PDW) state characterized by a spatially modulating density of electron pairs. Such a state should exhibit a periodically modulating energy gap $\Delta_P(\boldsymbol{r})$ in real-space, and a characteristic quasiparticle scattering interference (QPI) signature $\Lambda_P(\boldsymbol{q})$ in wavevector space. By studying strongly underdoped $Bi_2Sr_2CaDyCu_2O_8$ at hole-density ~0.08 in the superconductive phase, we detect the $8a_0$-periodic $\Delta_P(\boldsymbol{r})$ modulations signifying a PDW coexisting with superconductivity. Then, by visualizing the temperature dependence of this electronic structure from the superconducting into the pseudogap phase, we find evolution of the scattering interference

signature $\Lambda(\boldsymbol{q})$ that is predicted specifically for the temperature dependence of an $8a_0$-periodic PDW. These observations are consistent with theory for the transition from a PDW state coexisting with *d*-wave superconductivity to a pure PDW state in the $Bi_2Sr_2CaDyCu_2O_8$ pseudogap phase.

Introduction

1 Carrier-doped CuO_2 sustains both high temperature superconductivity and the pseudogap quantum fluid, often simultaneously. Although the former is reasonably well understood, a decades-long effort by physicists to identify the latter[1,2] has yet to bear fruit. The essential phenomenology of the pseudogap, while complex, is internally consistent. When *p* holes per unit-cell are introduced to CuO_2, the antiferromagnetic insulator (AF) state disappears and the pseudogap (PG) emerges in the region $p<p^*$ and $T<T^*(p)$ (Fig. 1a). For $T \lesssim T^*(p)$, an energy gap $\Delta^*(p)$ depletes the spectrum of electronic states, and thus the magnetic susceptibility[3] $\chi(T)$, the electronic specific heat[4] $C(T)$, the c-axis conductivity[5,6] $\rho(\omega, T)$, and the average density of electronic states[7] $N(E)$. In $\boldsymbol{k}$-space, there are four $\boldsymbol{k}(E = 0)$ Fermi arcs[8] neighboring $\boldsymbol{k} \approx (\pm\pi/2a, \pm\pi/2a)$, beyond which the 'pseudogap' $\Delta^*(\boldsymbol{k})$ opens[3,9,10] near $\boldsymbol{k} \approx (\pm\pi/a, 0); (0, \pm\pi/a)$. At extreme magnetic fields, tiny electron-like pockets with $\boldsymbol{k}$-space area $A_k \approx 7\%$ of the CuO_2 Brillouin zone, are detected[11] in the pseudogap state. Probes of electrical and thermal transport in the pseudogap phase evidence electron-pairs without phase rigidity[12,13,14]. Translational symmetry breaking is widely reported[15,16,17] to occur within the pseudogap phase; it is associated with charge density modulations of wavevectors $\boldsymbol{Q} \approx 2\pi/a\,(\pm 1/4, 0); (0, \pm 1/4)$. A 90^o-rotational (C_4)

symmetry breaking at $\boldsymbol{Q}$=0 and sometimes time-reversal symmetry breaking are also reported depending on materials and technique[18,19,20,21,22]. All these phenomena disappear[10,23,24] near a critical hole density $p = p^*$ which depends on material. The long-term challenge has been to identify a specific state of electronic matter that should exhibit all these properties simultaneously. A viable candidate has emerged recently[25-38], the pair density wave state[39].

2 A spatially homogeneous *d*-wave superconductor has an electron-pair potential or order parameter $\Delta_d(\boldsymbol{r}) = \Delta_0 e^{i\phi}$ with macroscopic quantum phase ϕ and critical temperature T_c. By contrast, a PDW state has an order parameter $\Delta_P(\boldsymbol{r})$ that modulates spatially at wavevectors $\boldsymbol{Q}_P$

$$\Delta_P(\boldsymbol{r}) = \left[\Delta(\boldsymbol{r})e^{i\boldsymbol{Q}_P\cdot\boldsymbol{r}} + \Delta^*(\boldsymbol{r})e^{-i\boldsymbol{Q}_P\cdot\boldsymbol{r}}\right]e^{i\theta} \quad (1)$$

with a macroscopic quantum phase θ. In theory, such a state exhibits a particle-hole symmetric energy gap $\Delta_P(\boldsymbol{k})$ near the BZ edges, with the $\Delta_P(\boldsymbol{k}) = 0$ points connected by extended $\boldsymbol{k}(E = 0)$ Fermi arcs[8,9,10]. Of necessity, such a partial gap suppresses $N(E)$, $C(T)$, $\chi(T)$, and $\rho(\omega, T)$. Moreover, a pure PDW is defined by a pair potential modulation as in equation (1) and exhibits a primary electron-pair density modulation $\rho_P(\boldsymbol{r}) = \rho_P^0\left[e^{i2\boldsymbol{Q}_P\cdot\boldsymbol{r}} + e^{-i2\boldsymbol{Q}_P\cdot\boldsymbol{r}}\right]$ along with a collateral charge density modulation $\rho_C(\boldsymbol{r}) = \rho_C^0\left[e^{i\boldsymbol{Q}_C\cdot\boldsymbol{r}} + e^{-i\boldsymbol{Q}_C\cdot\boldsymbol{r}}\right]$ with wavevector $\boldsymbol{Q}_C = \boldsymbol{2Q}_P$ (Ref. 39). If the PDW is unidirectional, it necessarily breaks the rotation symmetry of the material at $\boldsymbol{Q}$=0, and if biaxial it can break time reversal symmetry[40]. Finally, quasiparticles of the PDW should exhibit scattering interference signatures[35] which are uniquely characteristic of that state.

3 While charge density modulations $\rho_C(\boldsymbol{r})$ are widely reported in the pseudogap phase[15,16,17] it is unknown if electron-pair density $\rho_P(\boldsymbol{r})$ or electron-pair potential $\Delta_P(\boldsymbol{r})$ modulations exist therein. Whether the QPI signature $\Lambda_P(\boldsymbol{q})$ of a PDW occurs in the pseudogap phase is also unknown. Indeed, exploration of the pseudogap phase in search of a PDW poses severe experimental challenges. The modulating electron-pair density $\rho_P(\boldsymbol{r})$ which is iconic of the PDW state has been visualized directly by scanned Josephson tunneling microscopy[36,41] but such experiments must be carried out at sub-kelvin temperatures where both sample and STM tip are superconducting. Another approach used in the superconductive phase has been to visualize signatures of the PDW electron-pair potential modulations[35,37,38] $\Delta_P(\boldsymbol{r})$. But none of these experiments provide evidence on whether the pseudogap state in zero magnetic field is a PDW, because they were all carried out deep in the superconducting phase at temperatures $T \lesssim 0.1T_c$. At low temperatures but in high magnetic fields, both scanning tunneling microscopy and quantum oscillation studies report evidence for a PDW state[37,42], implying that the relict of suppressed superconductivity is a PDW. Therefore, our objective is to visualize the evolution with temperature of electronic structure, especially $\Delta_P(\boldsymbol{r})$ and $\Lambda_P(\boldsymbol{q})$, from the superconducting into the zero-field pseudogap phase of strongly underdoped $Bi_2Sr_2CaDyCu_2O_8$.

Results

4 For theoretical guidance, we use a quantitative, atomic-scale model for PDW state based upon CuO_2 electronic structure and the *t-J* Hamiltonian,

$$H = -\sum_{(i,j),\sigma} P_G t_{ij}\left(c_{i\sigma}^{\dagger}c_{j\sigma} + h.c.\right)P_G + J\sum_{<i,j>}\mathbf{S_i}\cdot\mathbf{S_j} \qquad (2)$$

Here, the electron hopping rates between nearest neighbor (NN) and next-nearest neighbor (NNN) Cu $d_{x^2-y^2}$ orbitals are t and t', respectively, the onsite repulsive energy $U \to \infty$, thus the antiferromagnetic exchange interactions $J=4t^2/U$, and the operator P_G eliminates all doubly-occupied orbitals. A renormalized mean-field theory (RMFT) approximation then replaces P_G with site-specific and bond-specific renormalization factors $g^t_{i,j}$ and $g^s_{i,j}$ based on the average number of charge and spin configurations permissible[34,35]. The resulting Hamiltonian is decoupled into a diagonalizable mean-field approximation using on-site hole density δ_i, bond field $\chi_{ij\sigma}$, and electron-pair potential $\Delta_{ij\sigma}$. The equations are initialized with a set of order parameter fields modulating at wavevector $\boldsymbol{Q}_P = (\pm 1/8, 0)2\pi/a_0$. In the self-consistent solution wavefunction $\Psi_0(\boldsymbol{r})$ of this broken-symmetry state then predicts the net charge on each Cu site $\delta_i = 1 - <\Psi_0|\sum_\sigma n_{i\sigma}|\Psi_0>$, the bond-field between adjacent sites i,j $\chi_{ij\sigma} = <\Psi_0|c^\dagger_{i\sigma}c_{j\sigma}|\Psi_0>$, and the electron-pair field on the bond between adjacent sites i,j $\Delta_{ij\sigma} = \sigma <\Psi_0|c_{i\sigma}c_{j\bar{\sigma}}|\Psi_0>$. Finally, because experimental visualizations are carried out at the crystal termination BiO layer of $Bi_2Sr_2CaDyCu_2O_8$, Cu $d_{x^2-y^2}$ Wannier functions $W_i(\boldsymbol{r})$ and lattice Green's function $G_{ij\sigma}(E)$ are used to generate the $\boldsymbol{r}$-space Green's functions $G_\sigma(\boldsymbol{r}, E) = \sum_{ij} G_{ij\sigma}(E) W_i(\boldsymbol{r}) W_j^*(\boldsymbol{r})$ everywhere at a height 0.4 nm above BiO terminal plane. Thus, the atomically resolved density of electronic states $N(\boldsymbol{r}, E) = \sum_\sigma -\frac{1}{\pi} \mathrm{Im}\, G_\sigma(\boldsymbol{r}, E)$ at the BiO termination surface of $Bi_2Sr_2CaDyCu_2O_8$ is predicted for the case where the adjacent CuO_2 crystal layer sustains a $\lambda = 8a_0$ PDW (Supplementary Note 1).

5 From this theory, Figure 2a shows the average $N(\boldsymbol{r}, E)$ at height ~4Å above the BiO termination in $Bi_2Sr_2CaDyCu_2O_8$ for the PDW state coexisting with d-wave superconductivity

(PDW+DSC state) at low-temperatures and pure PDW state at a higher temperature. The PDW+DSC state shows a V-shaped N(E) due to presence of nodes in DSC state. With increasing temperature the uniform component of the pair potential decreases (Supplementary Note 1 and Fig. 2e) and gap scales corresponding to DSC (Δ_0) and PDW (Δ_1) components can be identified as a shoulder feature and a coherence peak, respectively (light-blue curve corresponding to T=0.04t). Nodal points disappear in transition from PDW+DSC state to PDW state at higher temperatures leading to a large zero-energy N(E) in the latter (red curve corresponding to T=0.09t). These features agree with the experimental findings (Fig. 1d). However, the spectral gap defined by the position of the E>0 coherence peak reduces in the high-temperature PDW state due to the reduced $\Delta_{ij\sigma}$. We believe this discrepancy is a result of an inadequate treatment of self-energy effects in the current renormalized mean field theory, including the assumption of temperature independent Gutzwiller factors (Supplementary Note 1). Fig. 2b shows the most prominent Fourier components of the mean-fields in PDW+DSC and PDW states namely $\boldsymbol{Q_P} = (\pm 2\pi/8\, a_0, 0)$ and $\boldsymbol{Q_C} = \boldsymbol{2Q_P}$. All mean-fields, including the hole density and the *d*-wave gap order parameter[34] shown in Fig. 2c and 2d, respectively, exhibit periodicity of $8a_0$ in the PDW+DSC state at low temperatures. However, due to the absence of the uniform component ($\boldsymbol{q} = \boldsymbol{0}$) in pure PDW state, density-like quantities are $4a_0$ periodic as predicted by Ginzburg-Landau theories[39] (Fig 2c). The temperature dependence of the uniform and PDW ($\boldsymbol{q} = \boldsymbol{Q_P}$) components are shown in Fig. 2e. With increasing temperature, the uniform component of the gap, which corresponds to DSC in the PDW+DSC state, decreases rapidly and becomes negligibly small compared to the PDW component in the temperature range 0.05t<T<0.085t, but does not vanish. We have verified that a converged nonzero solution for

$\Delta(\boldsymbol{q}=0)$, 'fragile PDW+DSC' state', exists in this region (white background in Figs. 2e-f). For T>0.085t, the PDW+DSC solution of the RMFT equations becomes unstable and the pure PDW state is the only stable solution for a modulated state (pink background in Figs. 2e-f) (Supplementary Note 1). The temperature dependence of $\boldsymbol{q}=\boldsymbol{Q_P}$ and $\boldsymbol{q}=\boldsymbol{Q_C}$ components of the hole density is shown in Fig. 2f. We find that the $\boldsymbol{q}=\boldsymbol{Q_C}$ component of the charge density is dominant at all temperatures and the $\boldsymbol{q}=\boldsymbol{Q_P}$ component exhibits essentially the same temperature dependence as the uniform component of the gap order parameter. This is in agreement with Ginzburg–Landau theory[39] and experimental observation[37,38,41] that a PDW driven CDW will have $\boldsymbol{q}=\boldsymbol{Q_P}$ and $\boldsymbol{q}=\boldsymbol{Q_C}=\boldsymbol{2Q_P}$ components that are related to the uniform ($\Delta(\boldsymbol{0})$) and PDW ($\Delta(\boldsymbol{Q_P})$) components of the gap order parameter as $\delta(\boldsymbol{Q_P}) \propto (\Delta(\boldsymbol{0})\Delta(-\boldsymbol{Q_P})^* + \Delta(\boldsymbol{Q_P})\Delta(0)^*)$ and $\delta(\boldsymbol{Q_C}) \propto \Delta(\boldsymbol{Q_P})\Delta(-\boldsymbol{Q_P})^*$.

6 We explore these predictions using strongly underdoped $Bi_2Sr_2CaDyCu_2O_8$ samples with resistive transition temperature $T_c = 37 \pm 3\ K$ and $p \cong 0.08$ as shown schematically by the white arrow in Fig. 1a. These samples are cleaved in cryogenic vacuum at $T \approx 4.2K$ and inserted to the instrument. Measurements are carried out at a sequence of temperatures from $0.1T_c \leq T \leq 1.5T_c$ spanning the range from the superconducting to well into the pseudogap phase. The topographic images $T(\boldsymbol{r})$ of the FOV studied versus temperature (see "Methods" section; see also Supplementary Figure 2). Both the tip-sample differential tunneling current $I(\boldsymbol{r},V)$ and conductance $dI/dV(\boldsymbol{r},E=eV) \equiv g(\boldsymbol{r},V)$ are measured at bias voltage $V=E/e$ and with sub-angstrom spatial resolution. Because the density-of-electronic-states $N(\boldsymbol{r},E)$ is related to the differential conductance as $g(\boldsymbol{r},E) \propto N(\boldsymbol{r},E)[I_s/\int_0^{eV_s} N(\boldsymbol{r},E')dE']$, where I_s and V_s are arbitrary set-point parameters and the denominator

$\int_0^{eV_s} N(\boldsymbol{r},E')dE'$ is unknown, valid imaging of $N(\boldsymbol{r},E)$ is intractable. However, one can suppress these serious systematic "set-point" errors by using $R(\boldsymbol{r},E) = I(\boldsymbol{r},E)/I(\boldsymbol{r},-E)$ or $Z(\boldsymbol{r},E) = g(\boldsymbol{r},E)/g(\boldsymbol{r},-E)$ so that distances, modulation wavelengths and spatial-phases can be measured accurately. Furthermore, Bogoliubov scattering interference (BQPI) occurs when an impurity atom scatters quasiparticles, which interfere to produce characteristic modulations of $\delta N(\boldsymbol{r},E)$ surrounding each scattering site. The Fourier transform of $\delta N(\boldsymbol{r},E)$, $\delta N(\boldsymbol{q},E)$, then exhibits intensity maxima at a set of wavevectors of $\boldsymbol{q}_i$ connecting regions of high joint-density-of-states. Local maxima in $Z(\boldsymbol{q},E)$ therefore reveal the sets of energy dispersive wavevectors $\boldsymbol{q}_i(E)$ generated by the scattering interference. An efficient synopsis of these complex phenomena can then be achieved[10] by using $\Lambda(\boldsymbol{q},\Delta) = \sum_{E\cong 0}^{\Delta} Z(\boldsymbol{q},E)$, which provides a characteristic "fingerprint" of whatever ordered state, e.g. charge density wave (CDW) or PDW, controls the $\boldsymbol{q}_i(E)$.

7 At T = 4.2 K we first measure $g(\boldsymbol{r},V)$ in a 20 nm-square FOV (see "Methods" section and Supplementary Figure 2). The average differential conductance $g(V)$ is shown as a blue curve in Fig. 1d, where the energy of the coherence peak is determined from a local maximum in $g(V)$ for $V > 0$ (identified by a black vertical arrow). Measuring this energy versus location yields the so-called gapmap $\Delta_1(\boldsymbol{r})$ as shown in Fig. 3a. Fourier analysis of $\Delta_1(\boldsymbol{r})$ yields $\Delta_1(\boldsymbol{q})$, which exhibits significant disorder as $\boldsymbol{q} \to \boldsymbol{0}$ (Supplementary Figure 3b). But, by fitting the central peak to a cylindrical gaussian, and then subtracting it from $\Delta_1(\boldsymbol{q})$, we find four maxima at $\boldsymbol{q} \approx [(\pm 0.125 \pm 0.040, 0);\ (0, \pm 0.125 \pm 0.015)]\ 2\pi/a_0$ (inset in Fig 3a). These are the energy-gap modulations with period approximately $8a_0$, that have been previously reported[35, 37,38] for samples with $p \approx 0.17$, and are the signature of a PDW state

coexisting with *d*-symmetry superconductivity at low temperature. Fourier filtration of Fig. 3a retaining only modulations at $\boldsymbol{q} \approx [(\pm 1/8, 0);\ (0, \pm 1/8)]\ 2\pi/a_0$ yields an accurate image of the PDW gap modulations as seen in Fig. 3b. But when the same procedures are carried out at $\mathrm{T} = 1.5\mathrm{T}_C = 55$ K, the coherence peaks from which the gap is defined have so diminished that an equivalent gapmap is difficult to achieve. For example, Figs 3c and 3d show the measured $g(\boldsymbol{r}, 60\ mV)$ in an identical 10 nm-square FOV at $\mathrm{T} = 0.14\mathrm{T}_C = 5$ K and $\mathrm{T} = 1.5\mathrm{T}_C = 55$ K. Cross correlation analysis of $g(\boldsymbol{r}, V)$ at $\mathrm{T} = 0.14\mathrm{T}_C$ and of $g(\boldsymbol{r}, V)$ at $\mathrm{T} = 1.5\mathrm{T}_C$ in this FOV versus bias voltage V, yield a normalized cross correlation coefficients around 0.9 for practically all energies (Supplementary Note 3), thus indicating that virtually no changes have occurred in spatial arrangements of electronic structure upon entering the PG phase. The major exception is in the energy range $+100\ meV < E < +160\ meV$, wherein the feature denoted coherence peak (arrow Fig. 1d) diminishes strongly in amplitude. This however makes comparison of the $\Delta_1(\boldsymbol{r})$ in same FOV at T = 5 K and T = 55 K challenging. Figures 3e and 3f show the measured $\Delta_1(\boldsymbol{r})$ and, where it is possible to determine the energy, no changes have occurred in spatial arrangements of energy gaps either. The cross-correlation coefficient between the $\Delta_1(\boldsymbol{r}, 0.14T_C)$ and $\Delta_1(\boldsymbol{r}, 1.5T_C)$ is 0.685 indicating that the PDW state found at $\mathrm{T} \ll T_C$ remains robustly present at $1.5T_C$ deep into the pseudogap phase.

8 Next, we measure $g(\boldsymbol{r}, V, T)$ for $-34\ mV < V < 34\ mV$ at a sequence of temperatures $0.1T_c \leq T \leq 1.5T_c$. Then $Z(\boldsymbol{r}, V) = g(\boldsymbol{r}, +V)/g(\boldsymbol{r}, -V)$ is evaluated for each temperature, and the power-spectral-density Fourier transforms $Z(\boldsymbol{q}, V)$ are derived. Hence, $\Lambda(\boldsymbol{q}, \Delta_0) = \sum_{E \cong 0}^{\Delta_0} Z(\boldsymbol{q}, E)$ is calculated at each temperature where $\Delta_0 = 20\ meV$ is the observed energy above which dispersive scattering interference is no longer detectable[10,35]. The measured

temperature dependence of $\Lambda(\boldsymbol{q},\Delta_0)$ for $0.1T_c \leq T \leq 1.5T_c$ is shown in the left column in Fig. 4. The initial $\Lambda(\boldsymbol{q},\Delta_0)$ features at T=4.2K are exactly as expected from theory and as observed by experiment at p = 0.17, for a PDW coexisting with a *d*-wave superconductor[14]. As temperature increases the characteristics remain strikingly unchanged except that the intensity become significantly weaker. That the passage through T_c exhibits almost no signature in $\Lambda(\boldsymbol{q},\Delta_0)$, is unexpected if the scattering interference in $\Lambda(\boldsymbol{q},\Delta_0)$ is only due to the *d*-wave superconductivity. If however, a PDW state exists both below and above T_c this is what might logically be expected. Moreover, quantitative theoretical predictions for $\Lambda(\boldsymbol{q},\Delta_0)$ for a $\lambda = 8a_0$ PDW using the RMFT model, predict $N(\boldsymbol{q},E)$ surrounding a point-like scatterer and hence $\Lambda_P(\boldsymbol{q},\Delta_0) = \sum_{E\cong 0}^{\Delta_0} N(\boldsymbol{q},E)$ (Supplementary Note 5). Comparing our $\Lambda(\boldsymbol{q},\Delta_0)$ data to the RMFT-derived predictions $\Lambda_P(\boldsymbol{q},\Delta_0)$ for a $\lambda = 8a_0$ PDW in the right column in Fig. 4 shows how the key features in the experiments are reproduced in the theory over the whole range of temperatures. The implication is that the PDW state which definitely exists at lowest temperatures[35-38], continues to exist into pseudogap phase. But since that state is often (but not always) reported to support no supercurrents, it is possible that its PDW is in a strongly fluctuating regime[32,33,43-47].

9 Finally, we consider the widely promulgated hypothesis[15,16,17,] that it is predominantly a CDW state that breaks the translational symmetry of the cuprate pseudogap phase. First we note the very sharp distinction between these states: the mean-field order parameter of a PDW at wavevector $\boldsymbol{Q}_{\mathrm{P}}$ is $\langle c^{\dagger}_{\boldsymbol{k}\uparrow}\, c^{\dagger}_{-\boldsymbol{k}+\boldsymbol{Q}_{\mathrm{P}}\downarrow}\rangle$, whereas for a CDW at wavevector $\boldsymbol{Q}_{\mathrm{C}}$ it is $\sum_{\sigma}\langle c^{\dagger}_{\boldsymbol{k},\sigma} c_{\boldsymbol{k}+\boldsymbol{Q}_{\mathrm{C}},\sigma}\rangle$. Second, while a periodically modulating energy gap is a key PDW signature

(Fig. 3a), ***r***-space energy gap modulation should be weak in a CDW state, where it is charge density which modulates. Third, the quasiparticles and their scattering interference are highly distinct for the two states. Figure 5a shows the predicted $\Lambda_P(\boldsymbol{q}, \Delta_0) = \sum_{E\cong 0}^{\Delta_0} Z(\boldsymbol{q}, E)$ for a $\lambda = 8a_0$ PDW in the CuO_2 pseudogap phase, while Fig. 5b shows the equivalent predictions for a $\lambda = 4a_0$ CDW (Supplementary Note 5). In Fig. 5c,d we show the measured $\Lambda(\boldsymbol{q}, \Delta_0)$ at $T = 1.25T_c$ and $T = 1.5T_c$ ($\Lambda(\boldsymbol{q}, \Delta_0)$ analysis details are discussed in Supplementary Note 6). Clearly, the measured $\Lambda(\boldsymbol{q}, \Delta_0)$ is in superior agreement with the $\Lambda_P(\boldsymbol{q}, \Delta_0)$ signature of a $\lambda = 8a_0$ PDW rather than with that of a $\lambda = 4a_0$ CDW. The measured power-spectral-density Fourier transforms $Z(\boldsymbol{q}, V)$ are also in detailed agreement with the $Z(\boldsymbol{q}, V)$ of a $\lambda = 8a_0$ PDW (Supplementary Note 6). Finally, The $\Lambda(\boldsymbol{q}, \Delta_0)$ in the pseudogap phase forms an open contour near the lines $(\pm 1, 0)2\pi/a_0$ and $(0, \pm 1)2\pi/a_0$; this is consistent with the open contours in the $\Lambda_P(\boldsymbol{q}, \Delta_0)$ signature of a $\lambda = 8a_0$ PDW but distinct from the closed contours of a $\lambda = 4a_0$ CDW. Therefore, predictions of a pure PDW theory corresponds well and in detail to the complex patterns of the quasiparticle scattering that are actually observed in the pseudogap phase of $Bi_2Sr_2CaDyCu_2O_8$.

10 To summarize: strongly underdoped $Bi_2Sr_2CaDyCu_2O_8$ at $p \sim 0.08$ and T = 5 K exhibits the $8a_0$-periodic $\Delta_1(\boldsymbol{r})$ modulations characteristics of a PDW coexisting with superconductivity[35,37,38] (Fig. 2d, Fig 3b). Increasing temperature from the superconducting into the pseudogap phase, retains these real-space phenomena apparently thermally broadened but otherwise unchanged (Fig. 3c-f). More obviously, the measured scattering interference signature $\Lambda(\boldsymbol{q})$ evolves from correspondence with $\Lambda_P(\boldsymbol{q})$ predicted for an $8a_0$-periodic PDW coexisting with superconductivity[35] into that predicted for a pure $8a_0$-periodic

PDW above the superconductive T_c in the pseudogap phase (Fig. 4). Furthermore, this signature is highly distinct from $\Lambda(\boldsymbol{q})$ predicted for a $4a_0$-periodic CDW (Fig. 5). The clear inference from all these observations is that the $Bi_2Sr_2CaDyCu_2O_8$ pseudogap phase contains a robust PDW state.

Methods

Single crystals of $Bi_2Sr_2CaDyCu_2O_8$ with hole doping level of $p \approx 8\%$ and $T_c = 37\pm3$ K were synthesized using the floating zone method with doping controlled by oxygen depletion. The samples were cleaved in cryogenic ultrahigh vacuum at T = 4.2 K to reveal an atomically flat BiO surface, and then inserted into STM. All measurements are carried out using tungsten tips in a variable temperature (the range is T = 4.2 K – 55 K) spectroscopic imaging STM system with thermal fluctuations less than 1 mK. The PG gap map $\Delta_1(\boldsymbol{r})$ were measured with the resolution of 128 pixels × 128 pixels. The experimental parameters include setpoint voltage 800 mV, setpoint current 800 pA, bias voltage V_B = -800 mV – 800 mV and 161 discrete energy layers. The QPI images were measured with the resolution of 256 pixels × 256 pixels. The experimental parameters of the QPI measurements include spectroscopic setpoint voltage 200 mV, setpoint current 200 pA, bias voltage V_B = -34 mV – 34 mV and 35 discrete energy layers. The topography $T(\boldsymbol{r})$ of the six temperatures studied in this paper are shown in Supplementary Figure 2. The presented QPI patterns were symmetrized to reduce the noise. In the QPI pattern, a circle with a locus located at $\boldsymbol{q} = \boldsymbol{0}$ and a radius of 25 pixels is fitted to 2D Gaussian function and then removed.

Acknowledgements: The authors acknowledge and thank K. Fujita for very helpful discussions and advice. Y.X.C. and J.C.S.D acknowledge the Moore Foundation's EPiQS Initiative through Grant GBMF9457. J.C.S.D. acknowledge support from Science Foundation of Ireland under Award SFI 17/RP/5445. W.C. and J.C.S.D. acknowledge support Royal Society under Award R64897. S.W., W.R. and J.C.S.D. acknowledge support from the European Research Council (ERC) under Award DLV-788932. P.J.H. acknowledges support from research grant NSF-DMR-1849751.

Author Contributions: S.W., Y.X.C., W.C. and W.R. developed and implemented data analysis. P.C. and P.J.H carried out theoretical analysis. J.C.S.D. and P.H.H. conceived and supervised the project and wrote the paper, with key contributions from S.W. and P.C. H.E. and S.U. synthesized samples. The paper reflects contributions and ideas of all authors.

Competing Interests: The authors declare no competing interests.

Data and Materials Availability: Experimental details and data are available in the manuscript and the supplementary information.

FIGURES

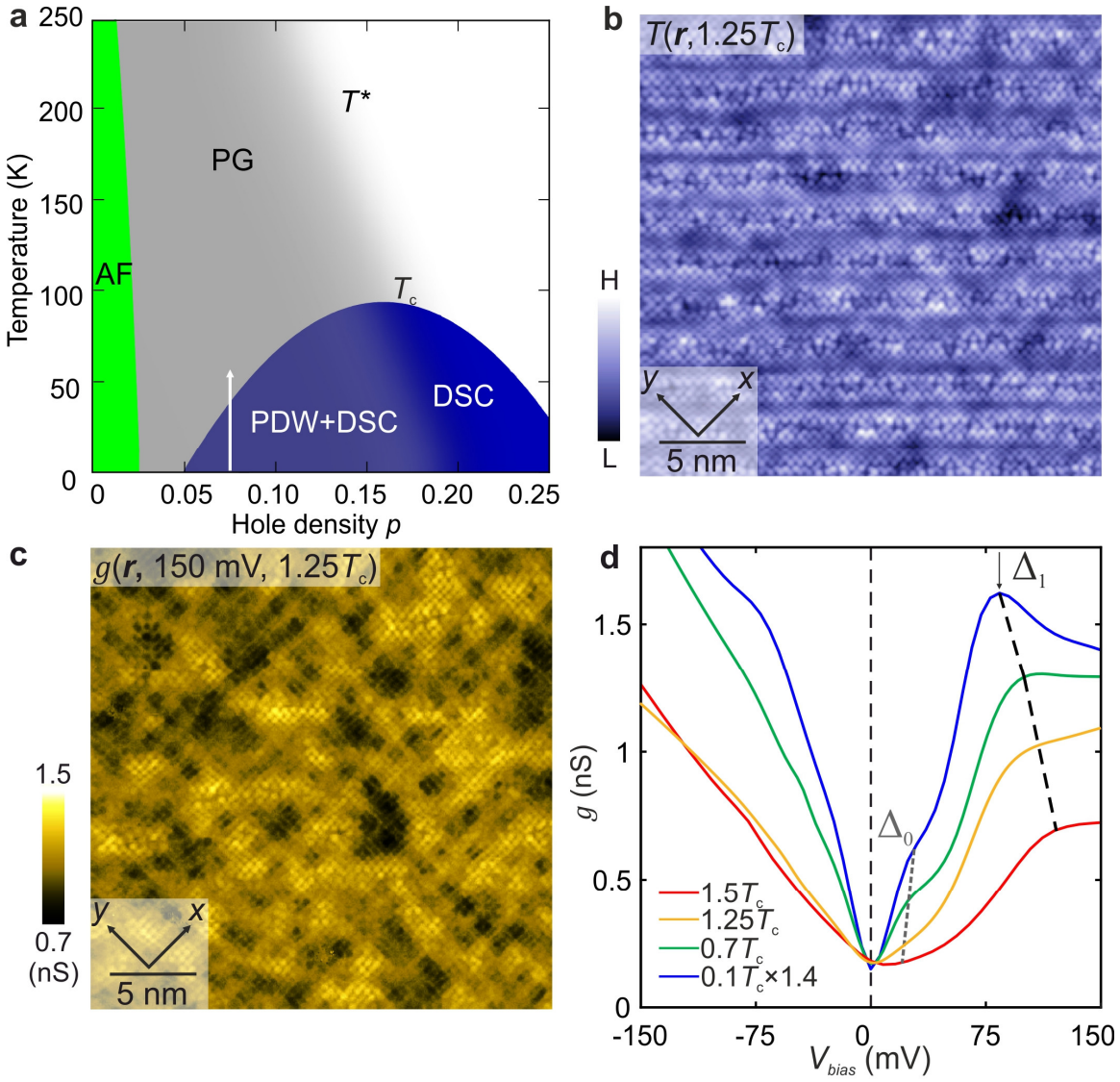

Figure 1

FIG. 1 Temperature dependence of cuprate broken-symmetry states.

a. Schematic phase diagram of hole-doped cuprates. The Mott insulator phase with long range antiferromagnetic order (AF) is replaced by the pseudogap phase (PG) with increasing hole doping p below the onset temperature T^*. The PG phase is characterized by the suppression of magnetic susceptibility, electronic specific heat, the c-axis conductivity and the average density of electronic states, and the appearance of a truncated Fermi surface. The d-symmetry Cooper-paired high-temperature superconductivity state (DSC) is indicated schematically in a blue "dome". The range of temperature T, in which the PG state is studied in this paper is indicated by the white arrow.

b. Topograph T(r) at the BiO termination layer at $T = 1.25T_c$ in the PG phase of $Bi_2Sr_2CaDyCu_2O_8$ for p ≈ 0.08.

c. Differential conductance map $g(\boldsymbol{r}, +150\text{ mV})$was obtained at the same field of view as B at $T = 1.25T_c = 45$ K. The g($\boldsymbol{r}$, E) manifests $\lambda = 4a_0$ charge modulations.

d. Evolution of the spatially averaged tunneling conductance spectra of $Bi_2Sr_2CaDyCu_2O_8$ with increasing T, here characterized by T_c. The gap $\Delta_1(T)$ is the energy of the coherence peak that is identified by a local maximum in g(V) for V>0 (indicated by a black vertical arrow). The energies $\Delta_0(T)$ (gray dashed line) are identified as the extinction energy of Bogoliubov quasiparticles using the method in Supplementary Note 5. The two characteristic energies $\Delta_0(T)$ and $\Delta_1(T)$ appear more subtle at higher temperatures due to thermal broadening. Note the tunneling spectra at 4.2 K (≈ $0.1T_c$) is multiplied by 1.4.

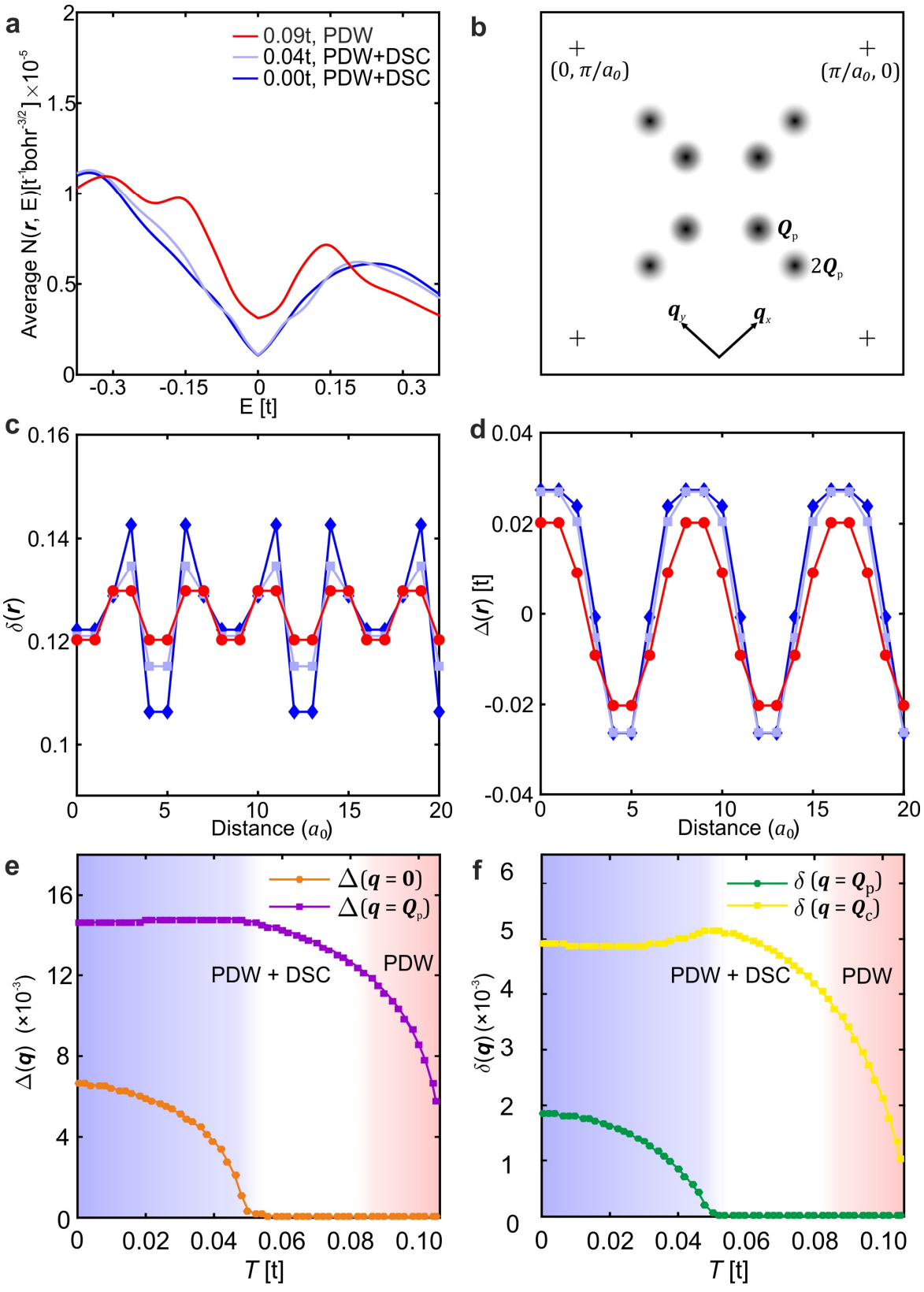
a
0.09t, PDW
0.04t, PDW+DSC
0.00t, PDW+DSC
Average N(r, E)[t⁻¹bohr⁻³²]×10⁻⁵
E [t]
b
(0, π/a₀)
(π/a₀, 0)
Q_p
2Q_p
q_y
q_x
c
δ(r)
Distance (a₀)
d
Δ(r) [t]
Distance (a₀)
e
Δ(q = 0)
Δ(q = Q_p)
PDW + DSC
PDW
Δ(q) (×10⁻³)
T [t]
f
δ (q = Q_p)
δ (q = Q_c)
PDW + DSC
PDW
δ(q) (×10⁻³)
T [t]

Figure 2

Fig. 2 Predicted temperature-evolution of the average local density of states (N(r)), hole density ($\boldsymbol{\delta}$) and d-wave gap order parameter ($\boldsymbol{\Delta}$) for the PDW state.

a. Continuum LDOS $N(\boldsymbol{r}, \mathrm{E})$ spatially averaged over a period of PDW ($8a_0$) at low-temperatures (T=0 and T=0.04t) and pure PDW state at a high temperature (T=0.09t) obtained using parameter set t = 400 meV, t' = -0.3t and J = 0.3t.. PDW+DSC state exhibits V-shaped nodal LDOS due to presence of the DSC component. Pure PDW state has Bogoliubov-Fermi pockets (in contrast to nodes in PDW+DSC state), which leads to a large E = 0 LDOS.

b. q-space schematic showing the most prominent wavevectors $\boldsymbol{Q}_P$ = [(±1/8, 0); (0, ±1/8)]$2\pi/a_0$ and $2\boldsymbol{Q}_P$ appearing in the Fourier transform of the mean-fields and other related quantities.

c. Spatial variation of hole density (δ) in PDW+DSC state (at T=0 and T=0.04t) and pure PDW state (at T=0.09t). Hole density modulates with a periodicity of $8a_0$ in PDW+DSC state due to presence of the DSC component and a periodicity of $4a_0$ in pure PDW state due to the absence of the DSC component, as expected from Ginzberg-Landau theories.

d. Spatial variation of d-wave gap order parameter in PDW+DSC state (at T=0 and T=0.04t) and pure PDW state (at T=0.09t) exhibiting $8a_0$-periodic modulations corresponding to the PDW component of the gap.

e. Temperature evolution of the uniform ($\boldsymbol{q} = \boldsymbol{0}$) and PDW ($\boldsymbol{q} = \boldsymbol{Q}_P$) components of the d-wave gap order parameter in PDW+DSC state (0<T<0.085t) and pure PDW state (0.085<T<0.11t). The uniform component of the gap decreases sharply with temperature becoming negligibly small, but finite, compared to the PDW component for 0.05t<T<0.085t. This 'fragile PDW+DSC' state is shown in white background. For T>0.085t PDW+DSC state becomes unstable and only pure PDW state (shown in pink background) exists as a stable solution of the RMFT equations.

f. Temperature evolution of the $\boldsymbol{q} = \boldsymbol{Q}_P$ and $\boldsymbol{q} = \boldsymbol{Q}_C = 2\boldsymbol{Q}_P$ components of hole density (δ) in PDW+DSC and pure PDW state in the same temperature range as in (e). The $\boldsymbol{q} = \boldsymbol{Q}_P$ component mirrors the temperature evolution of the uniform component of the gap (panel (e)), as expected from Ginzberg-Landau theories. $\boldsymbol{q} = \boldsymbol{Q}_C$ component is the dominant component at all temperature leading to $4a_0$–periodic charge density wave.

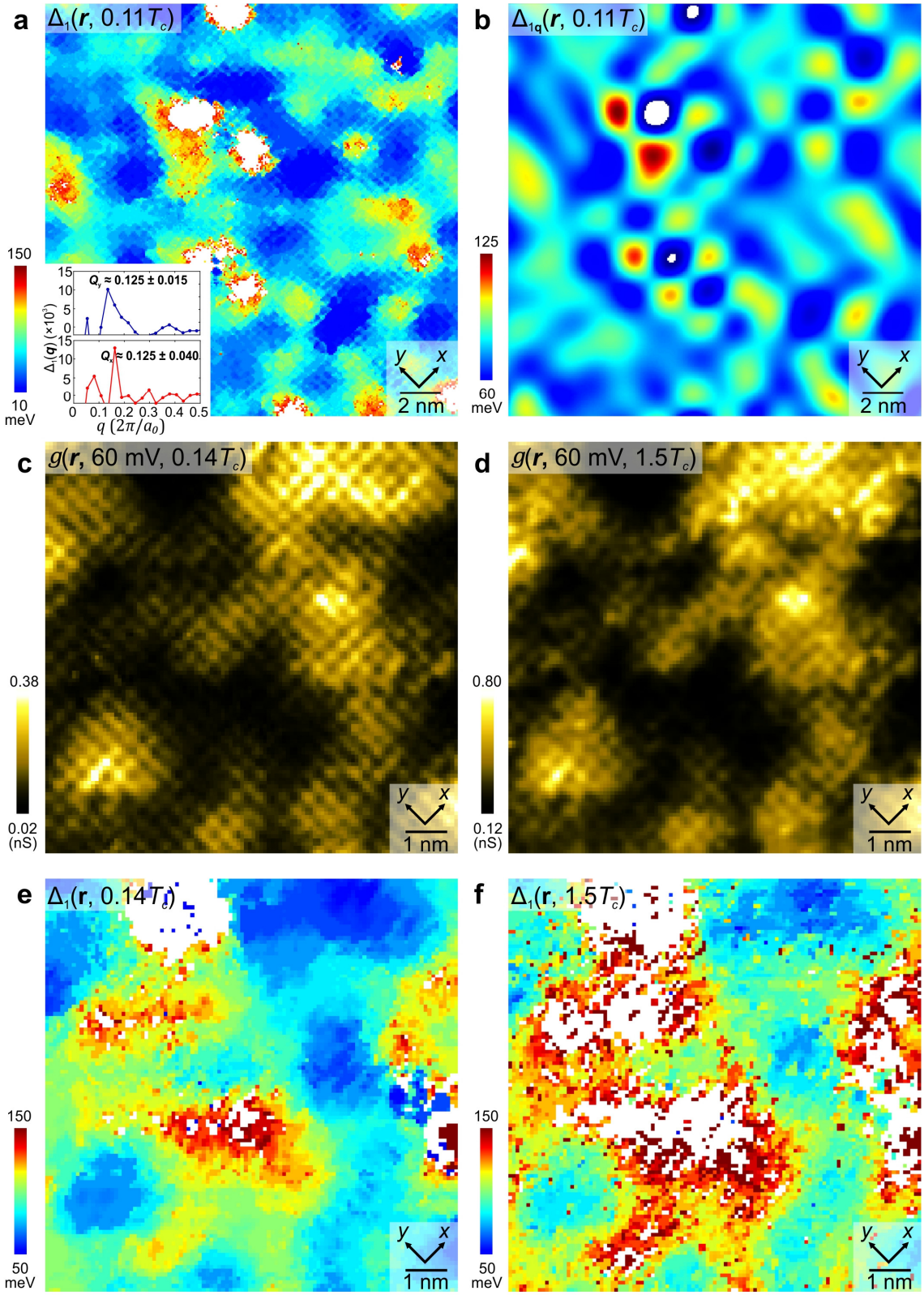
a
$\Delta_1(\boldsymbol{r}, 0.11T_c)$
150
10
meV
$Q_y \approx 0.125 \pm 0.015$
$Q_x \approx 0.125 \pm 0.040$
$\Delta_1(\boldsymbol{q})$ ($\times 10^3$)
q ($2\pi/a_0$)
y x
2 nm
b
$\Delta_{1q}(\boldsymbol{r}, 0.11T_c)$
125
60
meV
y x
2 nm
c
$g(\boldsymbol{r}, 60\text{ mV}, 0.14T_c)$
0.38
0.02
(nS)
y x
1 nm
d
$g(\boldsymbol{r}, 60\text{ mV}, 1.5T_c)$
0.80
0.12
(nS)
y x
1 nm
e
$\Delta_1(\mathbf{r}, 0.14T_c)$
150
50
meV
y x
1 nm
f
$\Delta_1(\mathbf{r}, 1.5T_c)$
150
50
meV
y x
1 nm

Figure 3

FIG 3. Energy-gap Modulations from Superconductive to Pseudogap Phase.

a. Measured $\Delta_1(\boldsymbol{r})$ within 20 nm × 20 nm FOV at T= $0.11T_C$ = 4.2K. The energy-gap is measured from the energy of the coherence peak at E > 0. The inset shows the linecuts from $\boldsymbol{q}$ = (0, 0) to (0.5, 0)$2\pi/a_0$ and from $\boldsymbol{q}$ = (0, 0) to (0, 0.5)$2\pi/a_0$ in the measured $\Delta_1(\boldsymbol{q})$ after subtraction of the disorder core. $\boldsymbol{q} \approx [(\pm 1/8, 0);\ (0, \pm 1/8)]\ 2\pi/a_0$ peaks are present in both directions. The white areas represent regions where it is impossible to determine the coherence peak position Δ_1.

b. Gap modulations $\Delta_{1q}(\boldsymbol{r})$ from 3(**a**). these are visualized at wavevectors $\boldsymbol{q} \approx [(\pm 1/8, 0);\ (0, \pm 1/8)]\ 2\pi/a_0$ by Fourier filtering $\Delta_1(\boldsymbol{r})$ at the 1/8 peaks as shown in inset of 3a.

c. Measured $g(\boldsymbol{r}, 60\ mV)$ at T = $0.14T_C$ = 5 K within 9.9 nm × 9.9 nm FOV. The $g(\boldsymbol{r}, 60\ mV)$ manifests unidirectional charge modulations.

d. Measured $g(\boldsymbol{r}, 60\ mV)$ at T = $1.5T_C$ = 55 K in the identical FOV as (**c**). No change has been detected in $g(\boldsymbol{r}, 60\ mV)$ at T = 55 K.

e. Measured $\Delta_1(\boldsymbol{r})$ at T= $0.14T_C$ = 5 K shows the spatial variation of the coherence peak at E > 0.

f. Measured $\Delta_1(\boldsymbol{r})$ at T = $1.5T_C$ = 55 K in the identical FOV as (**c**), (**d**) and (**e**). The spatial variation of the coherence peak is highly similar to (**e**).

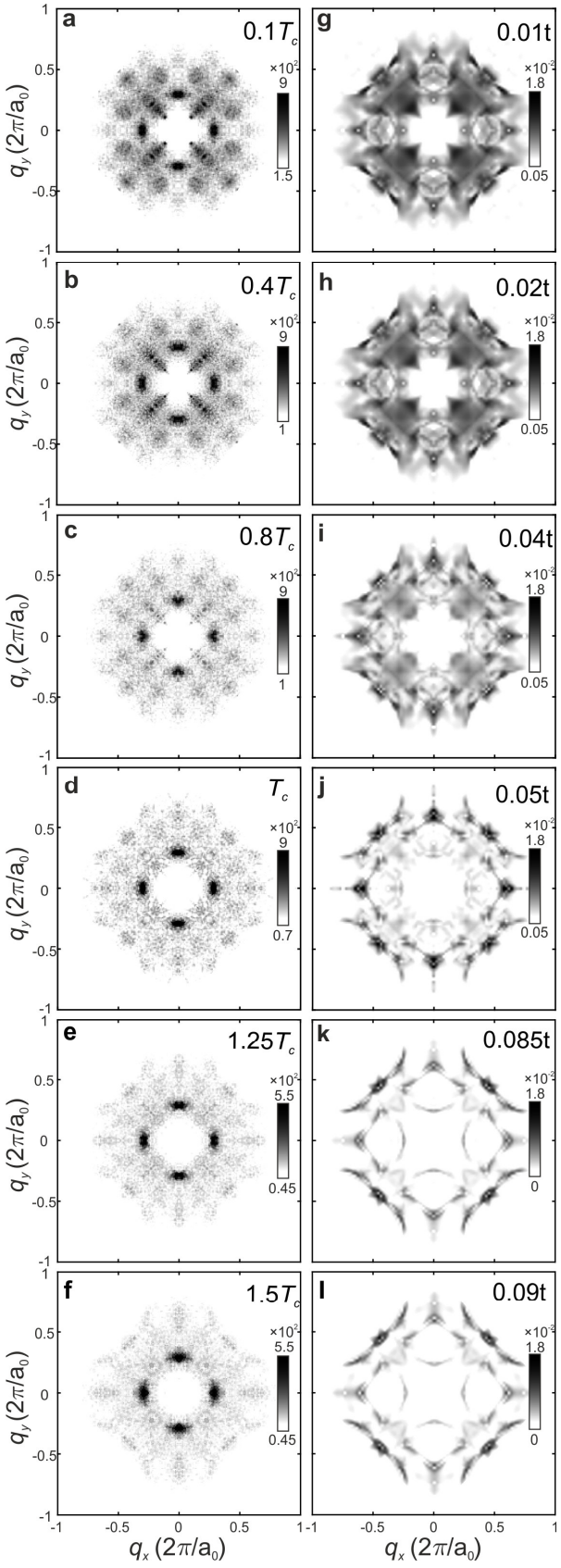
a
0.1T_c
g
0.01t
b
0.4T_c
h
0.02t
c
0.8T_c
i
0.04t
d
T_c
j
0.05t
e
1.25T_c
k
0.085t
f
1.5T_c
l
0.09t
q_y ($2\pi/a_0$)
q_x ($2\pi/a_0$)

Figure 4

FIG 4. Temperature Dependence of QPI Signature of a PDW

a-f. Measured QPI signature $\Lambda(\boldsymbol{q}, 20\ \text{meV})$ for $Bi_2Sr_2CaDyCu_2O_8$ (doping level p ≈ 0.08) at temperatures T = (**a**) $0.1T_c$, (**b**) $0.4T_c$, (**c**) $0.8T_c$, (**d**) T_c, (**e**) $1.25T_c$, and (**f**) $1.5T_c$.

g-j. Predicted QPI signature $\Lambda_P(\boldsymbol{q}, 20\ \text{meV})$ of $8a_0$ PDW state that coexists with DSC state at temperatures T = (**g**) 0.01t, (**h**) 0.02t, (**i**) 0.04t, and (**j**) 0.05t. Theoretically, it is assumed that discommensuration removes the Bragg peaks of the $4a_0$ density wave[48], so they are simply subtracted from predicted Λ_P of the commensurate state (Supplementary Note 4).

k-l. Predicted $\Lambda_P(\boldsymbol{q}, 20\ \text{meV})$ of pure $8a_0$ PDW state at temperatures T = (**k**) 0.085t and (**l**) 0.09t. Measured $\Lambda(\boldsymbol{q}, 20\ \text{meV})$ in (**a-f**) for $T = 0.1 \sim 1.5\ T_c$ are in good agreement with the simulation results in (**g-l**). The Fermi arc length increases from PDW+DSC to pure PDW state, which is a key feature of charge order driven by PDW. The intensity of $\Lambda(\boldsymbol{q})$ and $\Lambda_P(\boldsymbol{q})$ decreases as the temperature increases.

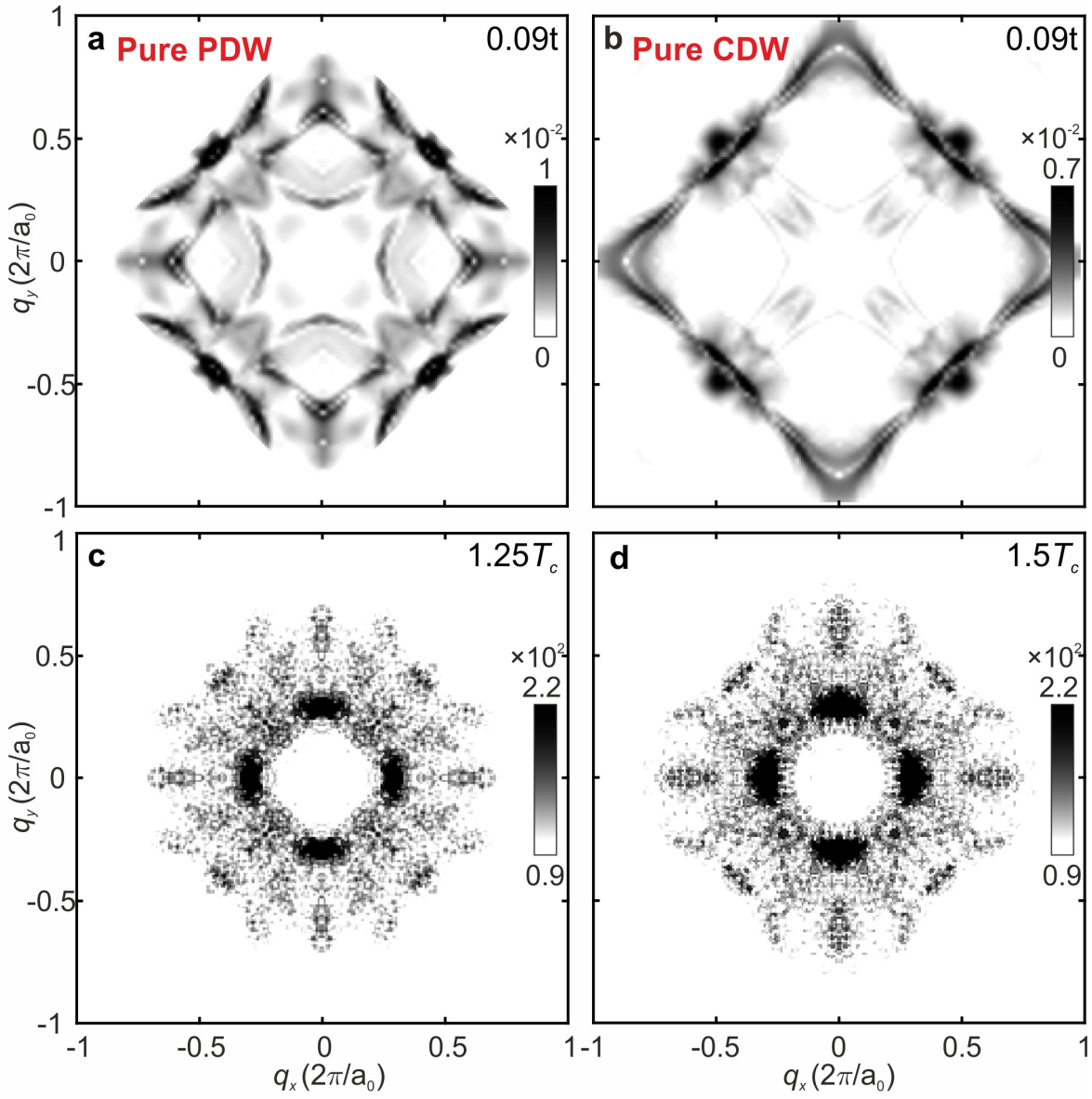
a Pure PDW
0.09t
×10^-2
1
0
b Pure CDW
0.09t
×10^-2
0.7
0
c
1.25T_c
×10^2
2.2
0.9
d
1.5T_c
×10^2
2.2
0.9
q_y (2π/a_0)
q_x (2π/a_0)
1
0.5
0
-0.5
-1

Figure 5

FIG 5. Discrimination of CDW from PDW QPI Signature in the Pseudogap State

a. Predicted QPI signature $\Lambda_P(\boldsymbol{q}, 20\text{ meV})$ of pure $8a_0$ PDW state at T = 0.09t. The PDW states show truncated Fermi surface.

b. Predicted $\Lambda_C(\boldsymbol{q}, 20\text{ meV})$ of pure $4a_0$ CDW state at T = 0.09t. The CDW states show very different features compared to the PDW state, such as a full Fermi surface.

c. Measured $\Lambda(\boldsymbol{q}, 20\text{ meV})$ of $Bi_2Sr_2CaDyCu_2O_8$ ($p \approx 0.08$) for the pseudogap phase at $T = 1.25T_c$.

d. Measured $\Lambda(\boldsymbol{q}, 20\text{ meV})$ of $Bi_2Sr_2CaDyCu_2O_8$ ($p \approx 0.08$) for the pseudogap phase at $T = 1.5T_c$. The measurements of the pseudogap phase agree much better with the pure PDW scenario (**a**) than with the pure CDW (**b**).

References

1 Norman, M. R., Pines, D. & Kallin, C. The pseudogap: Friend or foe of high T_c? *Adv. Phys.* **54**, 715–733 (2005).

2 Lee, P. A., Nagaosa, N. & Wen, X. G. Doping a Mott insulator: Physics of high-temperature superconductivity. *Rev. Mod. Phys.* **78**, 17–69 (2006).

3 Alloul, H., Ohno, T. & Mendels, P. 89Y NMR Evidence for a Fermi-Liquid Behavior in $YBa_2Cu_3O_{6+x}$. *Phys. Rev. Lett.* **63**, 1700–1703 (1989).

4 Loram, J. W., Mirza, K. . A., Cooper, J. R. & Liang, W. Y. Electronic specific heat of $YBa_2Cu_3O_{6+x}$ from 1.8 to 300 K J. *Phys. Rev. Lett.* **71**, 1740–1743 (1993).

5 Orenstein, J. *et al.* Frequency- and temperature-dependent conductivity in $YBa_2Cu_3O_{6+x}$ crystals. *Phys. Rev. B* **42**, 6342–6362 (1990).

6 Homes, C. C., Timusk, T., Liang, R., Bonn, D. A. & Hardy, W. N. Optical conductivity of c axis oriented $YBa_2Cu_3O_{6.70}$: Evidence for a pseudogap. *Phys. Rev. Lett.* **71**, 1645–1648 (1993).

7 Renner, C., Revaz, B., Genoud, J. Y., Kadowaki, K. & Fischer. Pseudogap precursor of the superconducting gap in under- and overdoped $Bi_2Sr_2CaCu_2O_{8+\delta}$. *Phys. Rev. Lett.* **80**, 149–152 (1998).

8 Norman, M. R. *et al.* Destruction of the Fermi surface in underdoped cuprates. *Nature* **392**, 157–160 (1998).

9 Loeser, A. G. *et al.* Excitation gap in the normal state of underdoped $Bi_2Sr_2CaCu_2O_{8+\delta}$. *Science* **273**, 325–329 (1996).

10 Fujita, K. *et al.* Simultaneous transitions in cuprate momentum-space topology and electronic symmetry breaking. *Science* **344**, 612–616 (2014).

11 Proust, C. & Taillefer, L. The remarkable underlying ground states of cuprate superconductors. *Annu. Rev. Condens. Matter Phys.* **10**, 409–429 (2019).

12 Corson, J., Mallozzi, R., Orenstein, J., Eckstein, J. N. & Bozovic, I. Vanishing of phase coherence in underdoped $Bi_2Sr_2CaCu_2O_{8+\delta}$. *Nature* **398**, 221–223 (1999).

13 Xu, Z. A., Ong, N. P., Wang, Y., Kakeshita, T. & Uchida, S. Vortex-like excitations and the onset of superconducting phase fluctuation in underdoped $La_{2-x}Sr_xCuO_4$. *Nature* **406**, 486–488 (2000).

14 Bollinger, A. T. *et al.* Superconductor-insulator transition in $La_{2-x}Sr_xCuO_4$ at the pair quantum resistance. *Nature* **472**, 458–460 (2011).

15 Fradkin, E., Kivelson, S. A. & Tranquada, J. M. Colloquium: Theory of intertwined orders in high temperature superconductors. *Rev. Mod. Phys.* **87**, 457–482 (2015).

16 Comin, R. & Damascelli, A. Resonant X-Ray scattering studies of charge order in cuprates. *Annu. Rev. Condens. Matter Phys.* **7**, 369–405 (2016).

17 Frano, A., Blanco-Canosa, S., Keimer, B. & Birgeneau, R. Charge ordering in superconducting copper oxides. *J. Phys. Condens. Matter* **32**, 374005 (2020).

18 Fauqué, B. *et al.* Magnetic order in the pseudogap phase of high-T_c superconductors. *Phys. Rev. Lett.* **96**, 197001 (2006).

19 Lawler, M. J. *et al.* Intra-unit-cell electronic nematicity of the high-T_c copper-oxide pseudogap states. *Nature* **466**, 347–351 (2010).

20 Shekhter, A. *et al.* Bounding the pseudogap with a line of phase transitions in $YBa_2Cu_3O_{6+\delta}$. *Nature* **498**, 75–77 (2013).

21 Sato, Y. *et al.* Thermodynamic evidence for a nematic phase transition at the onset of the pseudogap in $YBa_2Cu_3O_y$. *Nat. Phys.* **13**, 1074–1078 (2017).

22 Gupta, N. K. *et al.* Vanishing electronic nematic order beyond the quantum critical point in overdoped cuprate superconductors. *arXiv* 2012.08450 (2020).

23 Cooper, J. R., Loram, J. W., Kokanović, I., Storey, J. G. & Tallon, J. L. Pseudogap in $YBa_2Cu_3O_{6+\delta}$ is not bounded by a line of phase transitions: Thermodynamic evidence. *Phys. Rev. B* **89**, 201104 (2014).

24 Badoux, S. *et al.* Change of carrier density at the pseudogap critical point of a cuprate superconductor. *Nature* **531**, 210–214 (2016).

25 Berg, E. *et al.* Dynamical layer decoupling in a stripe-ordered high-T_c superconductor. *Phys. Rev. Lett.* **99**, 127003 (2007).

26 Lee, P. A. Amperean pairing and the pseudogap phase of cuprate superconductors. *Phys. Rev. X* **4**, 031017 (2014).

27 Berg, E., Fradkin, E. & Kivelson, S. A. Theory of the striped superconductor. *Phys. Rev. B.* **79**, 064515 (2009).

28 Berg, E., Fradkin, E., Kivelson, S. A. & Tranquada, J. M. Striped superconductors: How spin, charge and superconducting orders intertwine in the cuprates. *New J. Phys.* **11**, 115004 (2009).

29 Zelli, M., Kallin, C. & Berlinsky, A. J. Quantum oscillations in a π-striped superconductor. *Phys. Rev. B* **86**, 104507 (2012).

30 Norman, M. R. & Davis, J. C. S. Quantum oscillations in a biaxial pair density wave state. *Proc. Natl. Acad. Sci. U. S. A.* **115**, 5389–5391 (2018).

31 Caplan, Y. & Orgad, D. Quantum oscillations from a pair-density wave. *arXiv* 2103.01892 (2021).

32 Dai, Z., Senthil, T. & Lee, P. A. Modeling the pseudogap metallic state in cuprates: Quantum disordered pair density wave. *Phys. Rev. B* **101**, 064502 (2020).

33 Montiel, X., Kloss, T. & Pépin, C. Effective SU(2) theory for the pseudogap state. *Phys. Rev. B* **95**, (2017).

34 Choubey, P., Tu, W. L., Lee, T. K. & Hirschfeld, P. J. Incommensurate charge ordered states in the t-t′-J model. *New J. Phys.* **19**, 013028 (2017).

35 Choubey, P. *et al.* Atomic-scale Electronic Structure of the Cuprate Pair Density Wave State Coexisting with Superconductivity. *Proc. Natl. Acad. Sci. U. S. A.* **117**, 14805–14811 (2020).

36 Hamidian, M. H. *et al.* Detection of a Cooper-pair density wave in $Bi_2Sr_2CaCu_2O_{8+x}$. *Nature* **532**, 343–347 (2016).

37 Edkins, S. D. *et al.* Magnetic field-induced pair density wave state in the cuprate vortex halo. *Science* **364**, 976–980 (2019).

38 Du, Z. *et al.* Imaging the energy gap modulations of the cuprate pair-density-wave state. *Nature* **580**, 65–70 (2020).

39 Agterberg, D. F. *et al.* The physics of pair-density waves: cuprate superconductors and beyond. *Annu. Rev. Condens. Matter Phys.* **11**, 231–270 (2020).

40 Wang, Y., Agterberg, D. F. & Chubukov, A. Interplay between pair- and charge-density-wave orders in underdoped cuprates. *Phys. Rev. B* **91**, 115103 (2015).

41 Liu, X., Chong, Y. X., Sharma, R. & Davis, J. C. S. Discovery of a cooper-pair density wave state in a transition-metal dichalcogenide. *arXiv* 2007.15228 (2020).

42 Hsu, Y. *et al.* Unconventional quantum vortex matter state hosts quantum oscillations in the underdoped high-temperature cuprate superconductors. *Proc. Natl. Acad. Sci. U. S. A.* **118**, 2021216118 (2021).

43 Mross, D. F. & Senthil, T. Spin- and pair-density-wave glasses. *Phys. Rev. X* **5**, 031008 (2015).

44 Chan, C. Interplay between pair density waves and random field disorders in the pseudogap regime of cuprate superconductors. *Phys. Rev. B* **93**, 184514 (2016).

45 Chakraborty, D. *et al.* Fractionalized pair density wave in the pseudogap phase of cuprate superconductors. *Phys. Rev. B* **100**, 224511 (2019).

46 Lee, P. A. Proposal to measure the pair field correlator of a fluctuating pair density wave. *Phys. Rev. B* **99**, 035132 (2019).

47 Wårdh, J. Fluctuating superconductivity and pair-density wave order in the cuprate superconductors. (University of Gothenburg, 2020).

48 Mesaros, A. *et al.* Commensurate $4a_0$-period charge density modulations throughout the $Bi_2Sr_2CaCu_2O_{8+x}$ pseudogap regime. *Proc. Natl. Acad. Sci. U. S. A.* **113**, 12661–12666 (2016).

Supplementary Information for

Scattering Interference Signature of a Pair Density Wave State in the Cuprate Pseudogap Phase

Shuqiu Wang, Peayush Choubey, Yi Xue Chong, Weijiong Chen, Wangping Ren,

H. Eisaki, S. Uchida, P.J. Hirschfeld and J.C. Séamus Davis

Supplementary Note 1

Renormalized mean-field theory of the extended t-J model

For CuO_2 plane the t-J model is given by

$$H = -\sum_{(i,j),\sigma} P_G t_{ij}\left(c_{i\sigma}^{\dagger} c_{j\sigma} + h.c.\right)P_G + J\sum_{<i,j>} \boldsymbol{S}_i \boldsymbol{S}_j, \quad \text{(S1)}$$

where the hopping matrix elements t_{ij} are taken to be t for Cu-nearest neighbors (NN) and t' for next nearest neighbors (NNN), and J is their Heisenberg exchange. The operator P_G projects out doubly occupied sites from the Hilbert space. The Gutzwiller approximation to this model of strongly correlated electrons replaces the exact projection P_G with classical counting factors g^t and g^s depending on the allowed number of configurations of the degrees of freedom on a given site. This is determined by comparing expectation values of the kinetic and potential energies with their values taken in the Gutzwiller variational wavefunction.

This approach can be generalized to include a set of *local* renormalization factors, such that the renormalized Hamiltonian now reads,

$$H = -\sum_{(i,j),\sigma} g_{ij}^{t} t_{ij}\left(c_{i\sigma}^{\dagger} c_{j\sigma} + h.c.\right) + J\sum_{<i,j>}[g_{ij}^{S,Z} S_i^Z S_j^Z + g_{ij}^{S,xy}(\frac{S_i^{\dagger}S_j^{-} + S_i^{-}S_j^{\dagger}}{2})] \quad \text{(S2)}$$

where $< i,j >$ and (i,j) represent only NN, and both NN and NNN sites, respectively. Gutzwiller factors g^t and g^s then depend on the local mean fields. Once calculated in a self-consisted procedure, all physical observables can be obtained, and the locality of the fields allows the consideration of spatially modulated solutions to the mean field equations.

Mean-field decoupling of the renormalized Hamiltonian in Eq. S2 in pairing and density channels, and subsequent minimization of the ground state energy $E_g =< \Psi_0|H|\Psi_0 >$ with respect to the ground state wavefunction $|\Psi_0>$ leads to the following mean-field Hamiltonian[1]

$$H = \sum_{(i,j),\sigma} \epsilon_{ij\sigma} c^{\dagger}_{i\sigma} c_{j\sigma} + h.c. + \sum_{<i,j>,\sigma} \sigma D^{*}_{ij\sigma} c_{i\sigma} c_{j\bar{\sigma}} + h.c. - \sum_{i,\sigma} \mu_{i\sigma}\, n_{i\sigma}, \quad \text{(S3)}$$

where,

$$\epsilon_{ij\sigma} = -g^{t}_{ij} t_{ij} - \delta_{ij,<ij>} \tfrac{3}{4} J g^{S}_{ij} \chi^{*}_{ij\sigma} \quad \text{(S4)}$$

$$D_{ij\sigma} = -\delta_{ij,<ij>} \tfrac{3}{4} J g^{S}_{ij} \Delta_{ij\sigma} \quad \text{(S5)}$$

$$\mu_{i\sigma} = \mu + \tfrac{3}{4} J \sum_{j\sigma'} (\left|\Delta_{ij\sigma'}\right|^2 + |\chi_{ij\sigma'}|^2) \frac{dg^{S}_{ij}}{dn_{i\sigma}} + t_{ij} \sum_{j\sigma'} (\chi_{ij\sigma'} + \chi^{*}_{ij\sigma'}) \frac{dg^{t}_{ij}}{dn_{i\sigma}} \quad \text{(S6)}$$

Here, $\delta_{ij,<ij>}$ = 1 for NN sites and 0 otherwise. Various mean-fields appearing in the above equation are defined as

$$\Delta_{ij\sigma} = \sigma < \Psi_0 \left| c_{i\sigma} c_{j\bar{\sigma}} \right| \Psi_0 > \quad \text{(S7)}$$

$$\chi_{ij\sigma} = < \Psi_0 \left| c^{\dagger}_{i\sigma} c_{j\sigma} \right| \Psi_0 > \quad \text{(S8)}$$

$$\delta_i = 1 - < \Psi_0 | \sum_{\sigma} n_{i\sigma} | \Psi_0 > \quad \text{(S9)}$$

In writing Eq. S3, we have considered only paramagnetic states (m_i = 0) as we are interested in charge ordering without spin ordering. This significantly simplifies the expressions for Gutzwiller factors[1] as given below

$$g^{t}_{ij\sigma} = g^{t}_{ij} = g^{t}_{i} g^{t}_{j}; \; g^{t}_{i} = \sqrt{\tfrac{2\delta_i}{1-\delta_i}} \quad \text{(S10)}$$

$$g^{s,z}_{ij} = g^{s,xy}_{ij} = g^{s}_{ij} = g^{s}_{i} g^{s}_{j}; \; g^{s}_{i} = \tfrac{2}{1+\delta_i} \quad \text{(S11)}$$

Applying a Bogoliubov transformation diagonalizes the mean-field Hamiltonian in Eq. S3, and leads to the following BdG equation

$$\sum_j \begin{pmatrix} \epsilon_{ij\uparrow} & D_{ij\uparrow} \\ D^{*}_{ji\uparrow} & -\epsilon_{ij\downarrow} \end{pmatrix} \begin{pmatrix} u^{n}_{j} \\ v^{n}_{j} \end{pmatrix} = E_n \begin{pmatrix} u^{n}_{i} \\ v^{n}_{i} \end{pmatrix} \quad \text{(S12)}$$

which has to be solved self-consistently as the matrix elements depend on the mean-fields, which, in turn, are determined from the eigenvalues (u^{n}_{i}, v^{n}_{i}) and eigenvectors E_n. To obtain bond-centered PDW+DSC state as a self-consistent solution of Eq. S12, we initialize it with modulating bond-centered pair-field, keeping hole density and bond-field uniform, as follows

$$\Delta_{i,i+\hat{x}} = \Delta_0 + \Delta_Q \cos(\boldsymbol{Q}_P \cdot \mathbf{R}_i) \quad \text{(S13)}$$

$$\Delta_{i,i+\hat{y}} = -\Delta_0 - \Delta_Q \cos(\boldsymbol{Q}_P \cdot \mathbf{R}_i - \tfrac{\hat{x}}{2}) \quad \text{(S14)}$$

where $\boldsymbol{Q}_P = (1/8,0)2\pi/a_0$. To obtain pure PDW solution, we simply set $\Delta_0 = 0$. Results presented in the main-text were obtained using the parameter set t = 400 meV, t' = -0.3t and J = 0.3t.

We have assumed Gutzwiller factors to be independent from temperature and equal to their values at the temperature T = 0 (Eq. S10 and Eq. S11)[2]. The temperature dependence enters the computation via the Fermi function used in calculating expectation values of the mean-field parameters (Eq. S7-S9).

We initialized RMFT equations with appropriate seed as described above. We self-consistently obtain the stable PDW state in temperature range 0–0.11t and the PDW+DSC state in the temperature range 0–0.085t. Pure DSC state is the lowest energy paramagnetic solution of the *t-J* model. Both PDW and PDW+DSC states have almost equal energy per site, which is a few meV larger than the DSC state[1,3,4,5]. The tiny energy difference between PDW+DSC and DSC state can be overcome by a variety of means, such as disorder which is not accounted for in the calculation. We have assumed it to be true such that the PDW+DSC state is the ground state in the temperature range 0 – 0.085t, and for higher temperatures (in the range 0.085t – 0.11t), the pure PDW state becomes the ground state. In the PDW+DSC state, increasing temperature leads to a sharp decrease in the uniform DSC component ($\Delta(\mathbf{q}=0)$) as shown in the main-text Figure 2e. For 0.05t<T<0.085t, $\Delta(\mathbf{q}=0)$ is very small but finite. This 'fragile PDW+DSC' state is a stable solution of the RMFT equations and not a computational artefact. This result is verified by the observation that lowering the self-consistency tolerance by an order of magnitude yields the same state.

Using the eigenvalues and eigenvectors of the BdG matrix (Eq. S12), lattice Green's functions can be calculated using the following formula

$$G_{ij}(E) = g_{ij}^{t} \sum_{n} \frac{u_i^n u_j^{n*}}{\omega - E_n + i0^+} \tag{S15}$$

where, $0^+$is a small artificial broadening chosen to be 0.01t, and the sum runs over all the eigenvalues. The total LDOS at a lattice site is simply given by the imaginary part of the diagonal Green's function:

$$N_i(E) = -\frac{2}{\pi} Im[G_{ij}(E)], \tag{S16}$$

where the factor 2 accounts for spin degeneracy.

Differential conductance measured in an STM experiment is proportional to the LDOS at the tip position. Thus, we must compute LDOS at a continuum position for a meaningful comparison with the experimental data. This can be achieved by a basis transformation from lattice to continuum space where Wannier functions centered at the lattice sites serve as matrix elements of the transformation[6]. The resulting Green's function and LDOS in the continuum basis is given as

$$G(\boldsymbol{r}, \boldsymbol{r}'; E) = \sum_{ij} W_i(\boldsymbol{r}) G_{ij}(E) W_j^*(\boldsymbol{r}') \tag{S17}$$

$$N(\boldsymbol{r}, E) = -\frac{2}{\pi} Im[G_{ij}(\boldsymbol{r}, \boldsymbol{r}; E)] \tag{S18}$$

Here, $W_i(\boldsymbol{r})$ is the Wannier function centered at site *i*. To compute the continuum LDOS at a typical STM-tip height, we have employed Cu-$3d_{x2-y2}$ Wannier function obtained using Wannier90 package, same as in Ref. [4,7] and very similar to that in Ref. [8].

Supplementary Fig. 1a shows the continuum LDOS map at E = Δ_1 in the pure PDW state at T=0.09t. The LDOS shows a periodicity of $4a_0$. Supplementary Fig. 1b shows spectra at eight Cu positions marked in the panel 1a. Sharp features present at higher energies will be smeared by inelastic scattering, which has been shown to be necessary to account for the shape of spectra in underdoped cuprates[9]. We incorporate the effects of linear inelastic scattering by replacing the constant artificial broadening $i0^+$ by a bias-dependent term $i0^+ + i\Gamma$, where $\Gamma = \alpha|E|$. Using the experimental fits presented in Ref. [9], we set α = 0.25. Supplementary Fig. 1c shows the continuum LDOS incorporating the linear inelastic scattering. All LDOS (and quantities directly related to it) results presented in the main text have been obtained after accounting for the inelastic scattering.

Supplementary Note 2

PG gap $\Delta_1(\boldsymbol{r})$ modulation detection

We determine the gap map $\Delta_1(\boldsymbol{r})$ by measuring the energy of the coherence peak in each dI/dV spectrum at E > 0. Supplementary Figure 3b shows the magnitude of the power-spectral-density Fourier transform $\Delta_1(\boldsymbol{q})$ of the gap map $\Delta_1(\boldsymbol{r})$ in Figure 3a. There is strong disorder in $\Delta_1(\boldsymbol{q})$ surrounding $\boldsymbol{q} = 0$. In Supplementary Figure 3, we show $\Delta_1(\boldsymbol{q})$ intensities before and after the exponential background has been subtracted. After the background is subtracted, the maxima at $\boldsymbol{Q}_p \approx (2\pi/a_0)(0, \pm 1/8)$ and $\boldsymbol{Q}_p \approx (2\pi/a_0)(\pm 1/8, 0)$ become clearly visible. This analysis provides one type of experimental evidence of the $8a_0$ modulations in $\Delta_1(\boldsymbol{r})$.

Supplementary Note 3

Atomic precision image registration

In the temperature dependence experiments, $T(\boldsymbol{r}, 5\text{ K})$ and $T(\boldsymbol{r}, 55\text{ K})$ are measured in the same field of view with sub-unit-cell resolution. The data are processed by performing the Lawler-Fujita procedure[10] that maps the data onto a perfectly periodic lattice without lattice distortions. The data are subsequently corrected using shear transformation to maintain the C4 symmetry of the CuO_2 crystal lattice. After the topographs are corrected, $T(\boldsymbol{r}, 5\text{ K})$ and $T(\boldsymbol{r}, 55\text{ K})$ are registered to the exact same FOV with atom-by-atom precision as shown in Supplementary Figure 4a and b. Subtraction of $T(\boldsymbol{r}, 5\text{ K})$ from $T(\boldsymbol{r}, 55\text{ K})$ results in noise (Supplementary Figure 4c).

The differential conductance map $g(\boldsymbol{r}, V)$ is simultaneously acquired with $T(\boldsymbol{r})$. Applying the same image processing procedures of correcting $T(\boldsymbol{r})$ to $g(\boldsymbol{r}, V)$ gives rise to the temperature induced electronic structure changes. The electronic structures are measured in a wide energy range from -800 mV to 800 mV which includes the PG energy range. The cross-correlation coefficient between $g(\boldsymbol{r}, V)$ at 5 K and 55 K are around 0.9 in the large energy range (Supplementary Figure 4d). This method provides meaningful subtraction of high ($T > T_c$) and low ($T < T_c$) temperature data to detect temperature induced differences of the electronic structures at atomic scale.

Supplementary Note 4

Predicted temperature-evolution of gap map $\Delta_1(\boldsymbol{r})$

We calculated the temperature evolution of the gap map $\Delta_1(\boldsymbol{r})$. $\Delta_1(\boldsymbol{r})$ is defined as the energy of the coherence peak at E>0, i.e., the same definition as the experimental measurement in main-text Figure 3. The gap modulation in the PDW+DSC state has a periodicity of $8a_0$ (Supplementary Figure 5a and b). The amplitude of the y-averaged gap modulation is ~0.14t at T=0 and ~0.13t at T =0.04. The gap modulation in the pure PDW state has a periodicity of $4a_0$ (Supplementary Figure 5c). The amplitude of the y-averaged gap modulation is ~0.03t at T =0.09, which is much smaller compared to the PDW+DSC state. In this prediction the modulation periodicity of $\Delta_1(\boldsymbol{r})$ changes from $8a_0$ to $4a_0$ in the transition from the PDW+DSC state to the pure PDW state. In experiments we have observed that $\Delta_1(\boldsymbol{r})$ modulates at $8a_0$ (inset in main-text Figure 3a) at $T<<T_c$. However the modulation periodicity of $\Delta_1(\boldsymbol{r})$ could not be determined at T = 55 K = $1.5T_c$ due to the presence of large regions with indeterminate coherence peaks (see white regions in Figure 3f). Therefore the predicted temperature-evolution of the gap map $\Delta_1(\boldsymbol{r})$ could not be tested.

Supplementary Note 5

Bogoliubov quasiparticle scattering interference calculations

To compute Bogoliubov quasiparticle scattering interference (BQPI), we solve single-impurity scattering problem in the extended *t-J* model self-consistently. In presence of a point-like potential scatterer located at the lattice site *i**, the following Hamiltonian describes the system.

$$H = H_{t-J} + H_{imp},$$
$$H_{imp} = V_{imp} \sum_{\sigma} n_{i^*\sigma}, \quad \text{(S19)}$$

where, H_{t-J} is given by Eq. S1, and V_{imp} is the impurity potential. Inclusion of this impurity Hamiltonian modifies the mean-field equation S6 as $\mu_{i\sigma} \rightarrow \mu_{i\sigma} - V_{imp}\delta_{ii^*}$, (here

δ_{ij} is the Kronecker delta function) leaving everything else unchanged. The modified BdG equations are then solved self-consistently to yield pure PDW and PDW+DSC states in presence of an impurity at the origin. Subsequently, we compute continuum LDOS $N(\boldsymbol{r}, E)$ using the procedure described in Supplementary Note 1. To compute BQPI, we obtain Fourier transform of the $Z(\boldsymbol{r}, E)$ map at each E to obtain $Z(\boldsymbol{q}, E)$. Since, the continuum LDOS has intra-unit cell precision, BQPI at wavevectors in higher Brillouin zones are available, in contrast to the lattice LDOS-based calculations, which provide information about the wavevectors in the first Brillouin zone only. Supplementary Fig. 6a shows as obtained $Z(\boldsymbol{q}, E)$ map at a low bias $E = 0.1\Delta_1 (= 0.03t)$ in the PDW+DSC state at temperature $T = 0.04$t. The largest intensity occurs at the non-dispersing PDW Bragg wavevectors $\boldsymbol{q} = n\boldsymbol{Q}_P$, $n = \pm 0, \pm 1, \ldots, \pm 7$, making it hard to see the other dispersing wavevectors. We assume that the discommensuration present in the real material[11] will significantly reduce the intensity at the Bragg wavevectors, and suppress it "by hand" in the theoretical BQPI maps, as shown in Supplementary Fig. 6b. Moreover, to simulate the presence of domains with unidirectional density modulations along both x- and y-axes, we symmetrize the BQPI maps by adding their 90°-rotated versions, as shown in Supplementary Fig. 6c. All Λ-maps in PDW+DSC state and pure PDW state shown in the main-text (Fig. 4 and Fig. 5) and hereafter are obtained by following this procedure of Bragg peak suppression and four-fold symmetrization. The integrated $Z(\boldsymbol{q}, E)$ map, i.e. the $\Lambda(\boldsymbol{q})$ map provides an efficient way to identify the characteristic features of Cooper pairing in both underdoped and overdoped Cuprates[12]. The overdoped BSCCO shows a full Fermi surface-tracing trajectory, which is a hallmark of simple d-wave pairing and corresponding octet model[12]. In the case of underdoped BSCCO, only a part of the Fermi surface (an "arc") is observed when the $Z(\boldsymbol{q}, E)$ maps are integrated up to the uniform d-wave pairing gap scale Δ_0. No additional feature emerges if the upper limit of sum is set beyond Δ_0. We verify this by defining the Λ-map as a function of upper energy cut-off Δ_c:

$$\Lambda(\boldsymbol{q}, \Delta_c) = \sum_{E \cong 0}^{\Delta_c} Z(\boldsymbol{q}, \mathrm{E}) \qquad \text{(S20)}$$

The upper cut-off of energy integration Δ_c is set to 0.05t = 20 meV, where we have assumed t = 400 meV.

$\Lambda(\mathbf{q}, \Delta_c)$-maps in CDW states are constructed non self-consistently via two independent methods. The first method is setting gap order parameter in self-consistent PDW state to zero while keeping bond-order and on-site potential modulations intact (Supplementary Figure 7a). The other method is taking the normal state Hamiltonian from the uniform DSC state solution and adding a term producing a d-form factor bond ordered charge density wave (with $\mathbf{Q} = (1/4, 0)2\pi/a_0$) (Supplementary Figure 7b). The charge density wave has the same amplitude as the uniform DSC state gap field. These states become the same as in Supplementary Information section D of ref. [5] if the coexisting DSC state is removed. To calculate the Λ-maps, an impurity Hamiltonian is added and subsequently the corresponding Hamiltonians are diagonalized in the real space. This procedure is

equivalent to a T-matrix calculation. $\Lambda_c(\mathbf{q}, \Delta_c)$-maps of the pure CDW state obtained from both methods exhibit features very different from the $\Lambda(\mathbf{q}, \Delta_c)$ maps observed in experiments. We have presented $\Lambda_c(\mathbf{q}, \Delta_c)$ map from Supplementary Figure 7a in the main-text Figure 5b.

Supplementary Note 6

Energy-evolution of QPI signature of the pseudogap phase compared to the PDW state

To avoid the 'setup' effect in the experiments, we calculate the ratio of the total density of states

$$Z(\boldsymbol{r}, \mathrm{E}) \equiv \frac{g(\boldsymbol{r}, +\mathrm{E})}{g(\boldsymbol{r}, -\mathrm{E})} \tag{S21}$$

We take the power spectral density Fourier transform $Z(\boldsymbol{q}, \mathrm{E})$ of $Z(\boldsymbol{r}, \mathrm{E})$. The $Z(\boldsymbol{q}, \mathrm{E})$ are summed up to Δ_0, the energy that the Bogoliubov quasiparticles cease to exist[13]. Δ_0 is around 20 meV in the 8% hole-doped $Bi_2Sr_2CaDyCu_2O_8$ sample studied in this paper. The experimental $Z(\boldsymbol{q}, \mathrm{E})$ maps from 8 meV to 20 meV are in good agreement with the corresponding calculated $Z(\boldsymbol{q}, \mathrm{E})$ maps (Supplementary Figure 8).

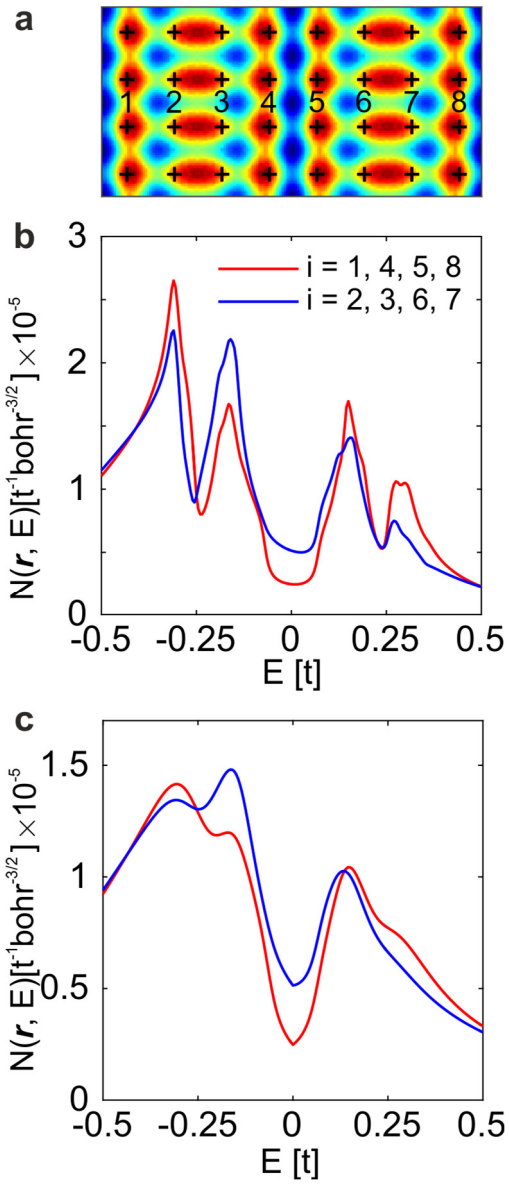

Supplementary Figure 1. Continuum LDOS in PDW state over a period of PDW ($8a_0$).
a. Continuum LDOS map N(r, E= Δ1) in the pure PDW state at T=0.09t over a $4a_0 \times 8a_0$ area, obtained using Eq. S18, for the same parameter set as in Fig. 2 of the main text. The location of a Cu atom is indicated by a black cross.
b. Continuum LDOS spectra N(r, E) above Cu positions, marked in the panel (a), without incorporating inelastic scattering.
c. Continuum LDOS spectra N(r, E) at the same positions as in (b), obtained after incorporating $\Gamma=\alpha|E|$ inelastic scattering ($\alpha=0.25$).

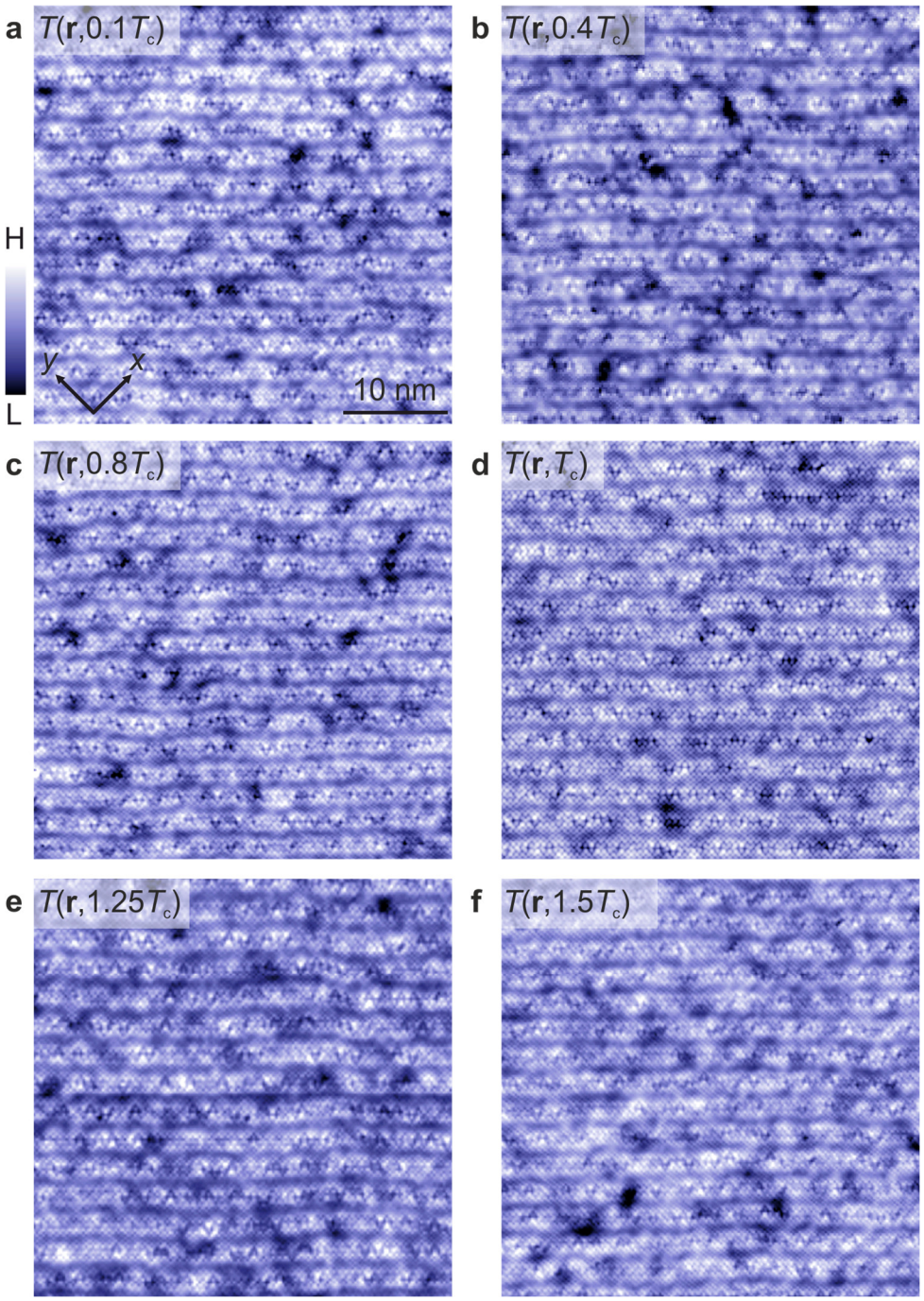

Supplementary Figure 2. Topography $T(\boldsymbol{r})$ within in a 40 nm × 40 nm FOV of the underdoped $Bi_2Sr_2CaDyCu_2O_8$ sample. The six QPI $\Lambda(\boldsymbol{q}, \Delta_0)$ maps from $0.1T_c$ to $1.5\ T_c$ are measured therein.

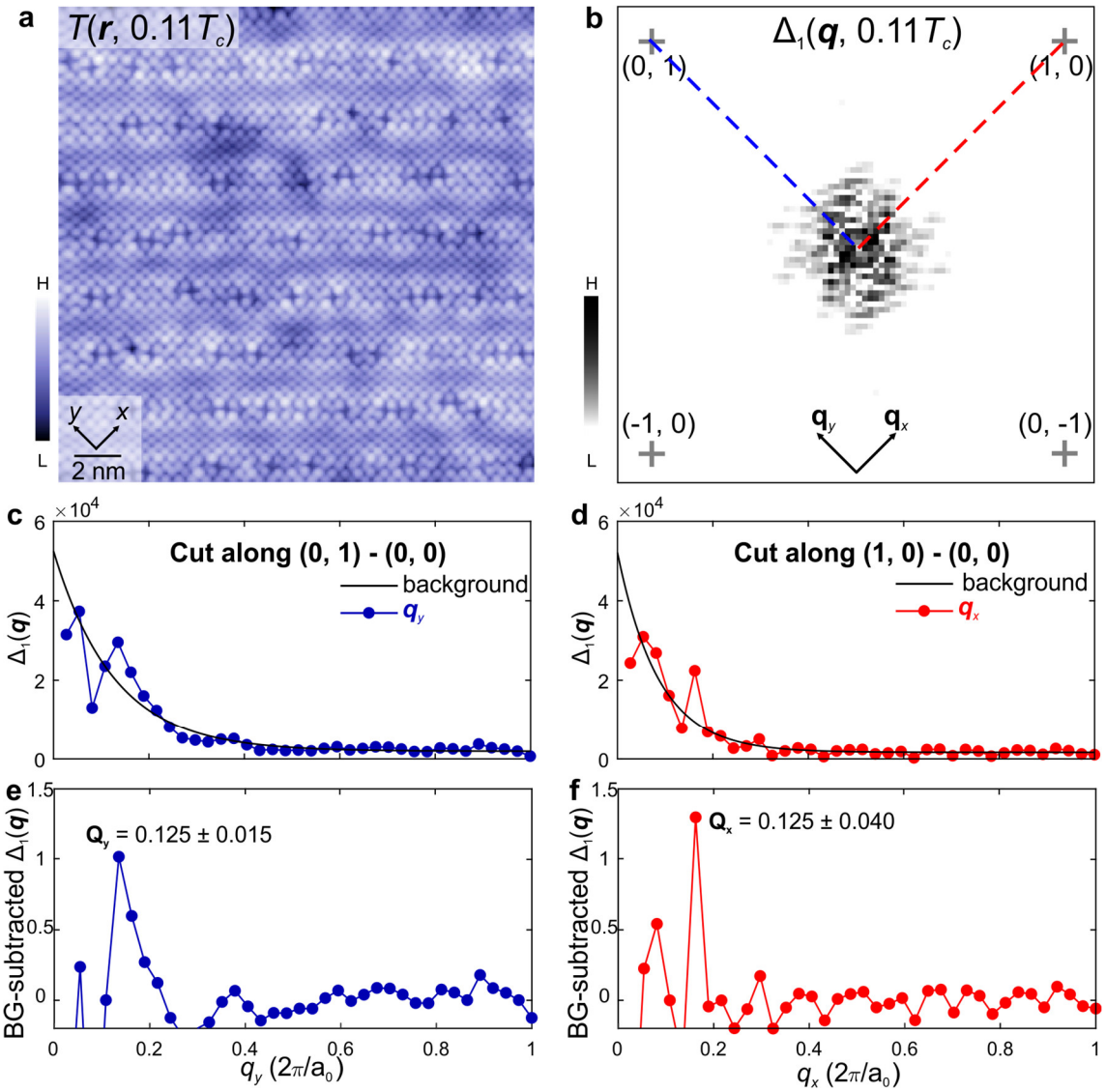

Supplementary Figure 3. Spatial variations and modulations in cuprate pseudogap energy gaps.

a. 20 nm × 20 nm topographic image $T(\boldsymbol{r})$ of BiO termination of $p \approx 8\%$ hole-doped $Bi_2Sr_2CaDyCu_2O_8$ surface at $T = 0.11T_C = 4.2K$. The gap map $\Delta_1(\boldsymbol{r})$ in Figure 3a in the main text is taken simultaneously from this FOV.

b. Amplitude Fourier transform $\Delta_1(\boldsymbol{q})$ *d*erived from the gap map $\Delta_1(\boldsymbol{r})$ at $T = 0.11T_C = 4.2K$ (Figure 3a in the main text).

c & **d**. Measured $\Delta_1(\boldsymbol{q})$ along (**c**) (0,0)-(0,1) and (**d**) (0,0)-(1,0). The linecut measurements are transverse average of 2 or 3 pixels. The measurements are subsequently fitted to an exponential background.

e & **f**. The same data as **c** & **d** but with the exponential background subtracted. The intensity due to the PG gap modulation is strongest at the $\boldsymbol{Q}_p \approx (2\pi/a_0)(0, \pm 1/8)$ that represents eight-unit-cell gap modulations in the *y* direction, and $\boldsymbol{Q}_p \approx (2\pi/a_0)(\pm 1/8, 0)$ that represents the gap modulations in the *x* direction.

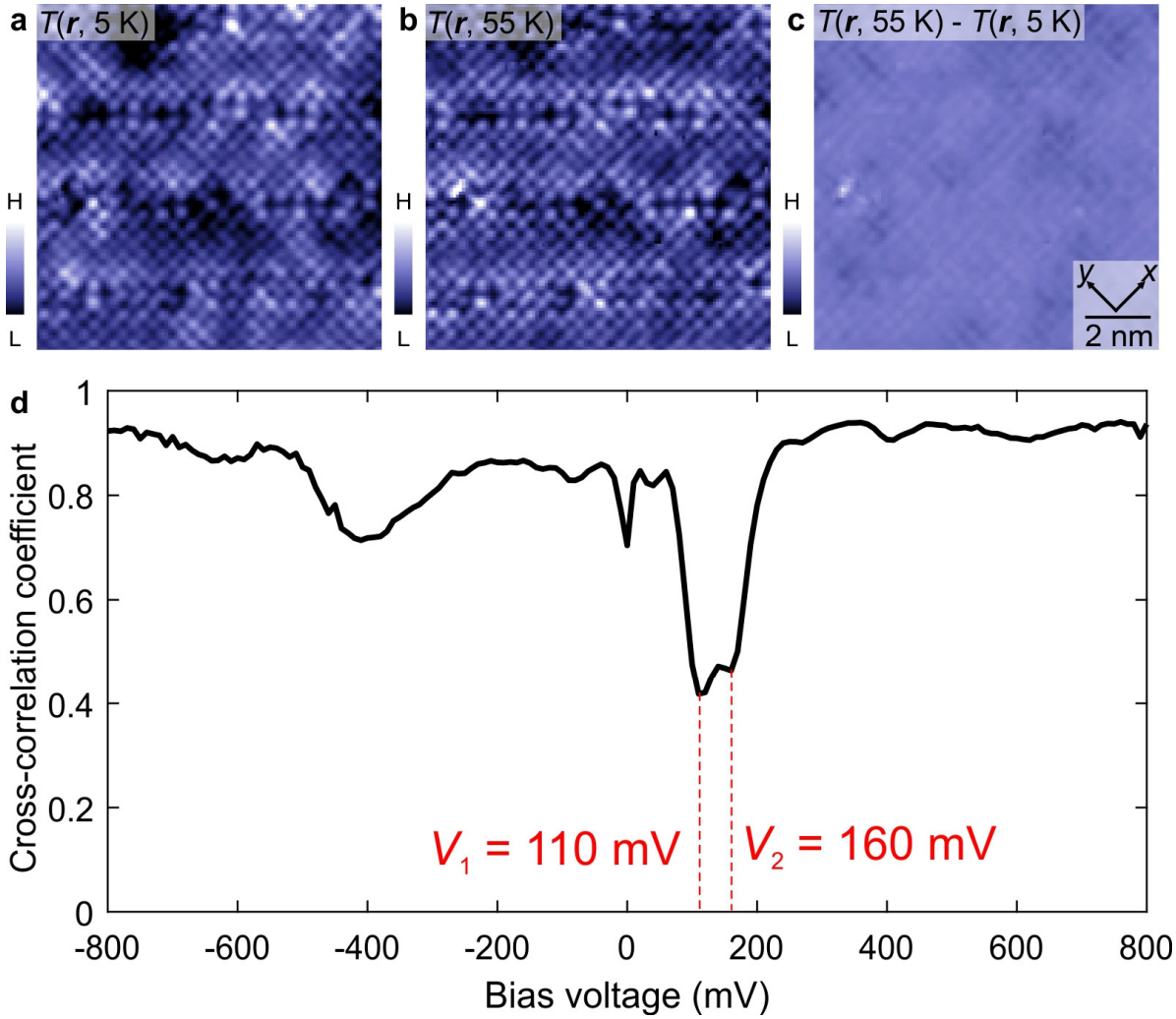

Supplementary Figure 4. Spatial registration of the two datasets at 5 K and 55 K.
a & **b**. $T(\boldsymbol{r}, 5\text{ K})$ and $T(\boldsymbol{r}, 55\text{ K})$ processed using the Lawler-Fujita algorithm. The distortions are now corrected and the CuO_2 lattice are identically periodic.
c. The difference between (**a**) and (**b**) is dominated by noise.
d. Cross-correlation coefficient between $g(\boldsymbol{r}, V, 5\text{ K})$ and $g(\boldsymbol{r}, V, 55\text{ K})$ as a function of bias voltage. There is strong correspondence between the two $g(\boldsymbol{r}, V)$ maps in the large energy scale except the PG energy gap scale from 110 to 160 mV.

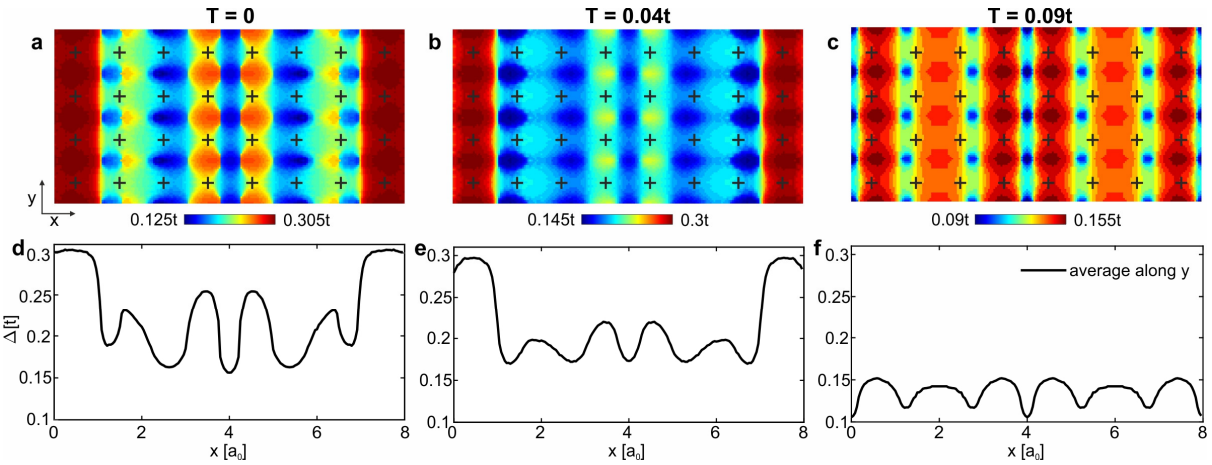

Supplementary Figure 5. Predicted temperature evolution of $\Delta_1(r)$ gap maps.

a-c. Gap maps in PDW+DSC state at (**a**) T = 0, (**b**) T = 0.04t, and in pure PDW state at (**c**) T = 0.09t over $8a_0 \times 4a_0$ area.

d-f. Gap averaged along y-axis (black).

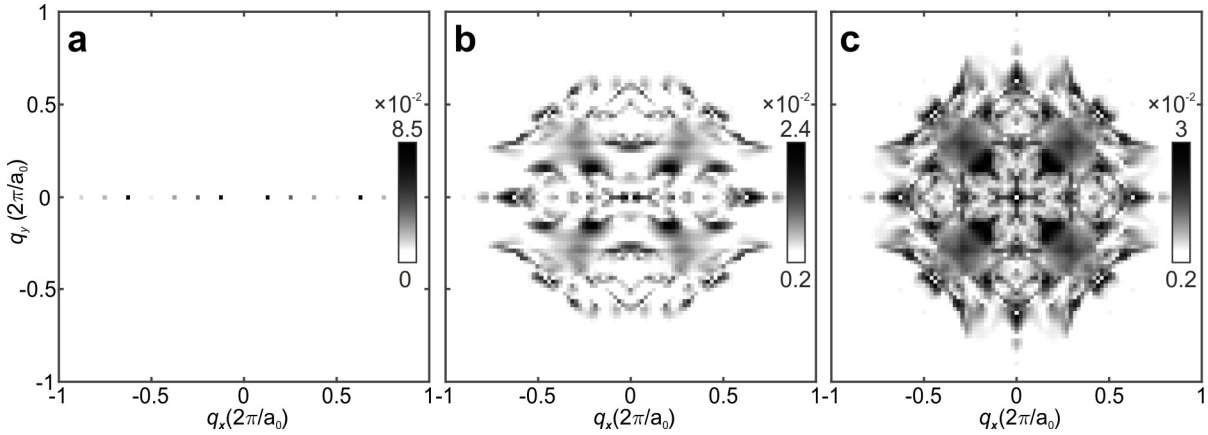

Supplementary Figure 6.

a. BQPI Z(***q***, E)-map at energy E = $0.1\Delta_1$ (=0.03t) in PDW+DSC state at temperature T = 0.04t obtained using parameters same as in Fig. 4 of the main text. Largest intensity occurs at non-dispersing Bragg peaks $\boldsymbol{q} = n\boldsymbol{Q_P}$, n = 0, 1, …, 7.

b. Same as in (**a**) with Bragg-peaks suppressed for a better visualization of dispersing wavevectors.

c. Symmetrized map obtained by adding the map in (**b**) and its 90° rotated version.

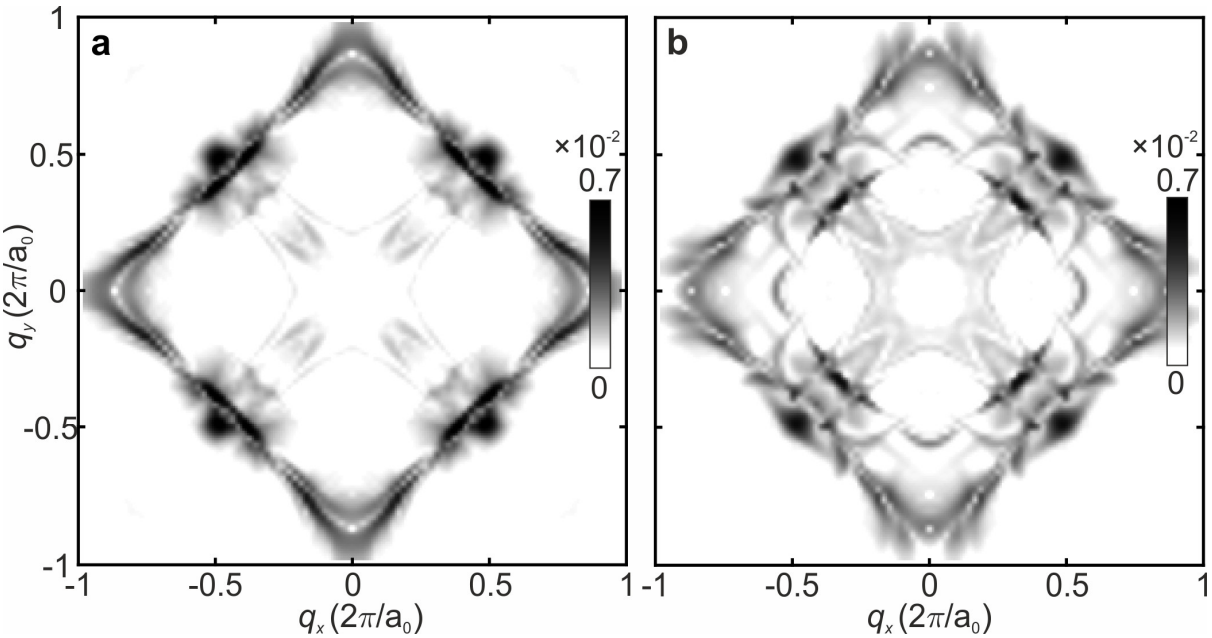

Supplementary Figure 7. $\Lambda_C(q, 20\ meV)$ for $4a_0$ CDW state constructed non self-consistently at temperature T = 0.09t.

a. $\Lambda_C(q, 20\ meV)$ for a CDW state constructed by setting the pair field to zero in the pure PDW state obtained self-consistently at T=0.09t.

b. $\Lambda_C(q, 20\ meV)$ for a CDW state constructed by taking the normal state Hamiltonian from the uniform DSC state solution at T=0.09t and, subsequently, adding a d-form factor charge density wave term.

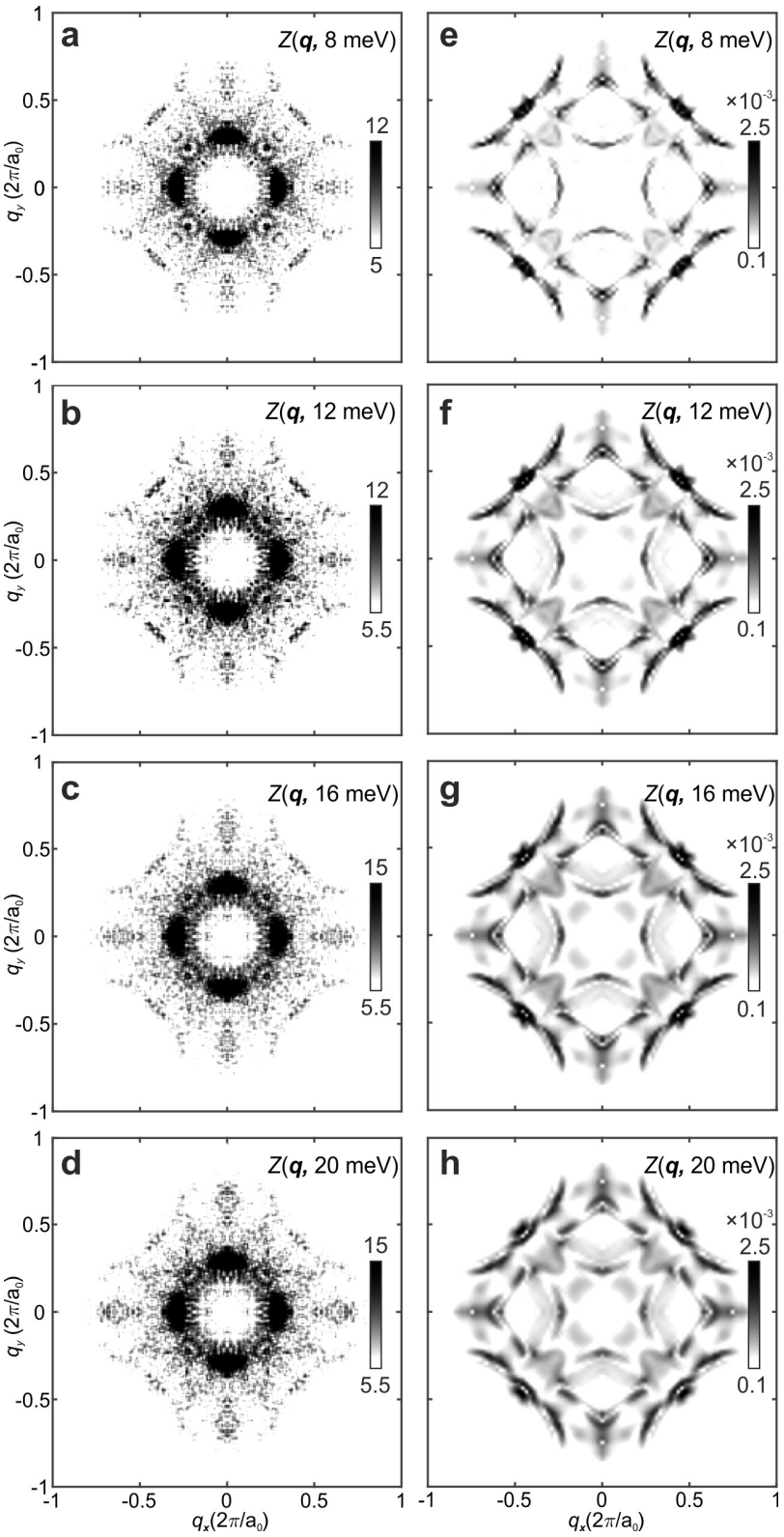

Supplementary Figure 8 Fourier transform Z(*q*, E) for a pure PDW state. The QPI signatures evolve dispersively with energy. (**a-d**) The experimental Z(***q***, E) maps taken at 55 K are in detailed agreement with (**e-h**) the theoretical Z(***q***, E) maps predicted for the pure PDW state obtained using the same parameters as in Fig. 5(a).

References

1 Yang, K. Y., Chen, W. Q., Rice, T. M., Sigrist, M. & Zhang, F. C. Nature of stripes in the generalized t-J model applied to the cuprate superconductors. *New J. Phys.* **11**, 055053 (2009)

2 Tu, W. L. & Lee, T. K. Evolution of pairing orders between pseudogap and superconducting phases of cuprate superconductors. *Sci. Rep.* **9**, 1719 (2019).

3 Tu, W. L. & Lee, T. K. Genesis of charge orders in high temperature superconductors. *Sci. Rep.* **6**, 18675 (2016).

4 Choubey, P., Tu, W. L., Lee, T. K. & Hirschfeld, P. J. Incommensurate charge ordered states in the t-t′-J model. *New J. Phys.* **19**, 013028 (2017).

5 Choubey, P. *et al.* Atomic-scale Electronic Structure of the Cuprate Pair Density Wave State Coexisting with Superconductivity. *Proc. Natl. Acad. Sci. U. S. A.* **117**, 14805–14811 (2020).

6 Choubey, P., Berlijn, T., Kreisel, A., Cao, C. & Hirschfeld, P. J. Visualization of atomic-scale phenomena in superconductors: Application to FeSe. *Phys. Rev. B.* **90**, 3–7 (2014).

7 Choubey, P., Kreisel, A., Berlijn, T., Andersen, B. M. & Hirschfeld, P. J. Universality of scanning tunneling microscopy in cuprate superconductors. *Phys. Rev. B* **96**, 174523 (2017).

8 Kreisel, A. *et al.* Interpretation of scanning tunneling quasiparticle interference and impurity states in cuprates. *Phys. Rev. Lett.* **114**, 1–6 (2015).

9 Alldredge, J. W. *et al.* Evolution of the electronic excitation spectrum with strongly diminishing hole density in superconducting $Bi_2Sr_2CaCu_2O_{8+\delta}$. *Nat. Phys.* **4**, 319–326 (2008).

10 Lawler, M. J. *et al.* Intra-unit-cell electronic nematicity of the high-T_c copper-oxide pseudogap states. *Nature* **466**, 347–351 (2010)..

11 Mesaros, A. *et al.* Commensurate $4a_0$-period charge density modulations throughout the $Bi_2Sr_2CaCu_2O_{8+x}$ pseudogap regime. *Proc. Natl. Acad. Sci. U. S. A.* **113**, 12661–12666 (2016).

12 Fujita, K. *et al.* Simultaneous transitions in cuprate momentum-space topology and electronic symmetry breaking. *Science* **344**, 612–616 (2014).

13 Kohsaka, Y. *et al.* How Cooper pairs vanish approaching the Mott insulator in $Bi_2Sr_2CaCu_2O_{8+\delta}$. *Nature* **454**, 1072–1078 (2008).